

Advances in Inkjet-Printed Metal Halide Perovskite Photovoltaic and Optoelectronic Devices

Florian Mathies,* Emil J. W. List-Kratochvil, and Eva L. Unger

Inkjet printing (IJP) has evolved over the past 30 years into a reliable, versatile, and cost-effective industrial production technology in many areas from graphics to printed electronic applications. Intensive research efforts have led to the successful development of functional electronic inks to realize printed circuit boards, sensors, lighting, actuators, energy storage, and power generation devices. Recently, a promising solution-processable material class has entered the stage: metal halide perovskites (MHPs). Within just 10 years of research, the efficiency of perovskite solar cells (PSCs) on a laboratory scale increased to over 25%. Despite the complex nature of MHPs, significant progress has also been made in controlling film formation in terms of ink development, substrate wetting behavior, and crystallization processes of inkjet-printed MHPs. This results in highly efficient inkjet-printed PSCs with a power conversion efficiency (PCE) of almost 21%, paving the way for cost-effective and highly efficient thin-film solar cell technology. In addition, the excellent optoelectronic properties of inkjet-printed MHPs achieve remarkable results in photodetectors, X-ray detectors, and illumination applications. Herein, a comprehensive overview of the state-of-the-art and recent advances in the production of inkjet-printed MHPs for highly efficient and innovative optoelectronic devices is provided.

defined as the repeatable generation of small droplets of a fluid and the subsequent deposition of these droplets onto a surface, as first described by Savart.^[1] Based on this general definition, IJP can be operated in a continuous or drop-on-demand (DoD) mode. Currently applied IJP techniques date back to the late 1940s when one of the first piezo-driven DoD devices was invented by Hansell.^[2] In the following years, technologies such as the very popular bubble jet technology, electrostatic DoD, liquid ink fault tolerant printing, and magnetic and acoustic IJP have been introduced.^[3]

Despite the wide variety of inkjet systems, printing of materials relevant for printed electronic and optoelectronic materials (metal nanoparticles, metal-organic precursors, conjugated polymers, etc.) almost exclusively rely on piezo-driven DoD inkjet printheads. This is because DoD printheads allow using of aqueous and organic solvent-based inks, at a wide range of viscosities, enabling a high inte-

gration density of printheads in industrial processes. A printer system accessing productivities of up to $6 \text{ m}^2 \text{ min}^{-1}$ while maintaining small printed feature sizes of $\approx 10 \text{ }\mu\text{m}$. By this means, IJP can thus be utilized to process all layers of an electronic or optoelectronic device as demonstrated on a research level over the past 30 years for organic and now hybrid semiconductor-based devices.^[4–8] Utilization of IJP stretches of course beyond material science. As an example in medicine, IJP of living cells has been utilized for tissue engineering.^[9] Due to this versatility and the mentioned advantages, there is the prospect that currently established standard processes can be replaced in various industries by this innovative contactless layer or material

1. Introduction

Inkjet printing (IJP) is familiar to most people in the form of desktop office printers. Yet, over the past 30 years, IJP has been established as a reliable, mature, and cost-effective production technology in many industrial sectors ranging from the graphic arts to the electronics industry. This is because IJP is a purely additive, digital, mask-less direct writing technique, and consumes a minimum amount of material in the production process. IJP processes are highly flexible, which enable customized prototype production as well as inline and roll-to-roll (R2R) manufacturing with a low capital investment barrier. IJP is

Dr. F. Mathies, Dr. E. L. Unger
Young Investigator Group Hybrid Materials Formation and Scaling
Helmholtz-Zentrum Berlin GmbH
Kekuléstrasse 5, 12489 Berlin, Germany
E-mail: florian.mathies@helmholtz-berlin.de

 The ORCID identification number(s) for the author(s) of this article can be found under <https://doi.org/10.1002/ente.201900991>.

© 2019 The Authors. Published by WILEY-VCH Verlag GmbH & Co. KGaA, Weinheim. This is an open access article under the terms of the Creative Commons Attribution License, which permits use, distribution and reproduction in any medium, provided the original work is properly cited.

DOI: 10.1002/ente.201900991

Dr. E. L. Unger
Chemical Physics and Nano Lund
Lund University
P.O. Box 124, Lund 22100, Sweden

Prof. E. J. W. List-Kratochvil
Humboldt-Universität zu Berlin
Institut für Physik, Institut für Chemie
IRIS Adlershof
Brook-Taylor-Straße 6, 12489 Berlin, Germany

Prof. E. J. W. List-Kratochvil
Helmholtz-Zentrum
Berlin für Materialien und Energie GmbH
Brook-Taylor-Straße 6, 12489 Berlin, Germany

deposition method. This technological breakthrough is emerging in the display industry, where organic light-emitting diodes (OLEDs) are fabricated using IJP.^[10] With the expertise of manufacturers of inkjet printers such as Kateeva Inc.,^[11] and light-emitting materials such as Merck, DuPont and Sumitomo,^[12] display producers such as JOLED, Samsung, and BOE^[13] are moving to IJP technique for the realization of next-generation displays.

Along these lines, printed solar cells are in the focus of many scientific and early-stage industrial undertakings. The promise of being able to manufacture large-area printed components, with high-throughput rates and with minimal precious material deposited, and thus at low cost, is appealing to manufacture solar energy conversion devices and IJP has been demonstrated as organic,^[14–16] kesterite,^[17–22] chalcopyrite,^[23–26] and now, also as metal halide perovskite (MHP) solar cells.

In recent years, MHPs have been one of the most exciting research topics for scientists of a wide variety of backgrounds. Mainly driven by photovoltaics (PV), the exceptional optical and electrical properties of MHPs engender power conversion efficiencies (PCEs) of over 25% on a laboratory scale.^[27] The ease of fabrication from solution and the broad range of possible applications promises MHP to achieve a strong market presence as a low-cost semiconductor material.^[28] One of the major challenges is the upscaling of MHP solar cells. As attention has turned from improving the PCE of laboratory perovskite solar cells (PSCs) toward upscaling PSC to commercial scale, more reports have emerged that are compatible with high-throughput manufacturing processes derived from printing technology. Even these printing methods are more likely to be adopted for commercial production of PSCs and modules, less attention has been focused on them relative to spin coating, and thus the overall state of the art in PCE of the resulting devices is lower. This includes also the increasing difficulty in producing defect-free films for larger cell size. Nevertheless, recent advances with large-area deposition processes, e.g., IJP, have demonstrated that achieving reasonable PCE for commercial-scale devices is a realistic goal and is more limited by process engineering challenges rather than by fundamental scientific obstacles. IJP has been identified by other groups as a major contributor as scalable process technology toward commercialization of PSCs.^[29–31] In addition to the use in PV, inkjet-printed MHPs have an impact on lighting and sensor applications.

This Review highlights the various possibilities of inkjet technology for MHP-based devices and applications. Device performance and printing results are connected through the so-called golden triangle of IJP: the combination of ink, substrates, and printing parameters, as shown in **Figure 1a**. Following a more general introduction to IJP, this Review focuses on the different process parameters governing the fabrication of efficient MHP-based devices. The progress in IJP utilized to manufacture solar cell, lighting, and sensing devices will be summarized in detail and guidelines are provided to enable further optimization of IJP as a process technique for the deposition of MHP semiconductors. This Review closes with a summary and outlook about current challenges and next



Florian Mathies received his doctoral degree in electrical engineering from the Karlsruhe Institute of Technology, focusing on inkjet printing of metal halide perovskites for photovoltaic and lighting applications. Before that, he obtained his B.Sc. and M.Sc. in physics from the University of Heidelberg, while working at the interdisciplinary research platform InnovationLab on printed organic electronics. In 2018, he joined Eva Unger's Young Investigator Group at Helmholtz-Zentrum Berlin as a postdoctoral researcher, focusing on formation and scaling of printed PSCs. Within the HySPRINT InnovationLab he is collaborating with Emil J.W. List-Kratochvil from Humboldt-University zu Berlin strengthen his knowledge on hybrid devices.



Emil J. W. List-Kratochvil received his doctoral degree in experimental solid-state physics (2000) from the Graz University of Technology, where he completed his habilitation in solid-state physics (2003). Between 2006 and 2015, he was appointed as Scientific Managing Director of the NTC Weiz GmbH. Since 2015, he is professor at the Humboldt-Universität zu Berlin, focusing on

structure to property relationships in (printed) organic and hybrid semiconductor devices. He currently works on electronic and optoelectronic components, additive resource-efficient deposition techniques, and in situ nanostructuring and synthesis methods. Since 2018, he is leader of the joint research group Generative Production Processes for Hybrid Components at the Helmholtz-Zentrum Berlin.



Eva L. Unger studied chemistry at the University of Marburg (2007) and received a doctoral degree in physical chemistry from the Uppsala University (2012) where she worked on excitonic dye solar cells. During her postdoctoral work at the Stanford University (2012–2014), she started working on perovskite solar cells as an early adaptor. Since 2016, she is an assistant senior lecturer at the Lund

University, where she collaborates on rationalizing photo-physical phenomena in metal-halide perovskite semiconductors. Since 2017, she is leading a Young Investigator Group within the HySPRINT Innovation Lab at the Helmholtz-Zentrum Berlin, focusing on scaling and rationalization of solution-based metal-halide perovskite deposition processes.

steps to enable moving forward from research to industrial utilization of MHP semiconductors.

2. Inkjet Printing

2.1. Fundamentals of IJP

In a piezo-DoD printer, the fluid is maintained at ambient pressure, and a piezo-transducer is used to create a drop only

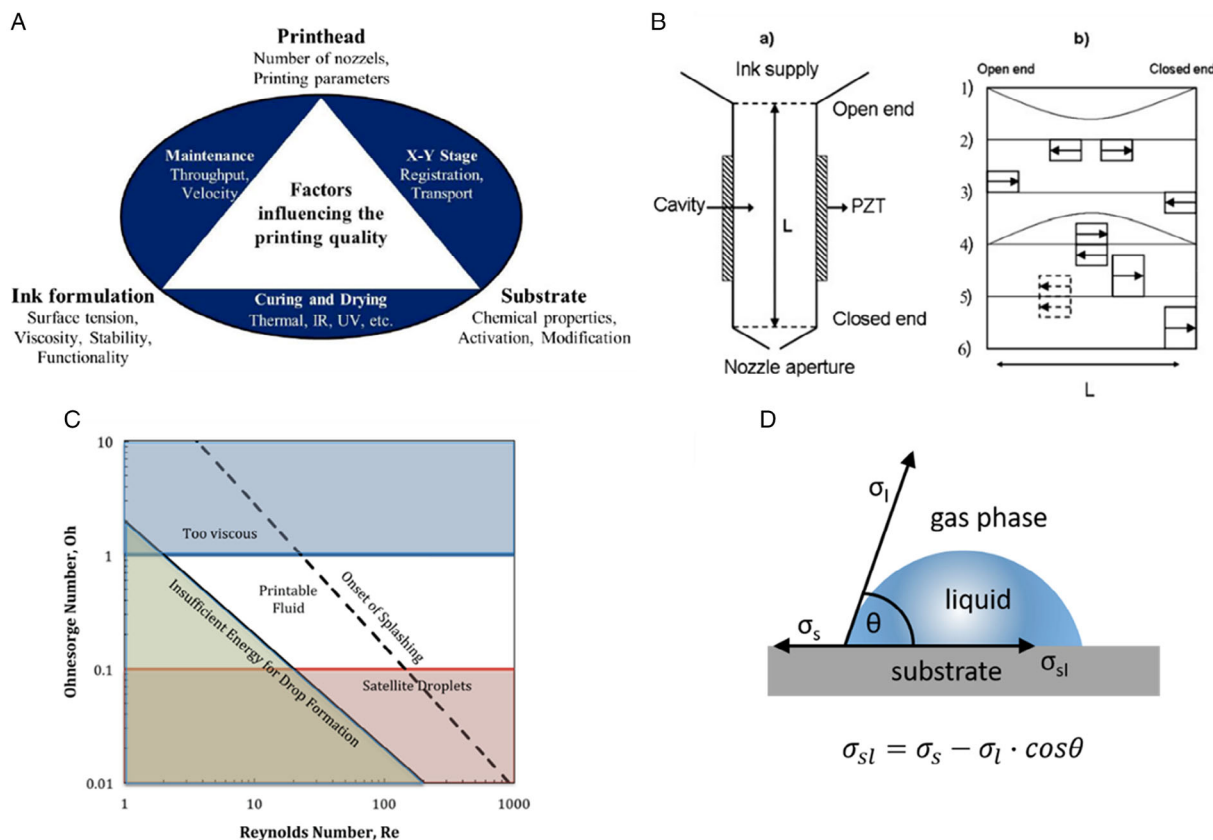


Figure 1. a) The “Magic Triangle of Inkjet Printing Technology.” Ink formulation, printhead, and substrate influence the printing quality. Reproduced with permission.^[32] Copyright 2015, SPIE. b) Piezoelectric inkjet printhead and schematic representation of wave propagation and reflection in a piezoelectric tubular actuator. Reproduced with permission.^[8] Copyright 2018, Royal Society of Chemistry. c) Regime of fluid properties allowing for DoD IJP. Reproduced with permission.^[33] Copyright 2011, AIP Publishing. d) Scheme of Young’s equation.

when needed. Such systems were first described by Hansell in the late 1940s.^[2] For successful drop formation, the transfer of kinetic energy from the transducer to the ink must be large enough to overcome the surface tension at the nozzle. An excitation pulse in the range of about 1–100 μs creates a volumetric change in the fluid which in turn induce different pressure waves, which undergo constructive and destructive interference traveling through the printhead (see Figure 1b). Upon constructive interference, a drop is being ejected at the orifice. Such systems can achieve typical drop velocities of 8–10 ms^{-1} and allow for a variation of the drop column between 5 and 80 pl. Typical printing frequencies of the printheads are between 10 and 40 kHz. The final droplet size will depend on the diameter of the orifice, usually in the range from 25 to 125 μm , whereas the resolution achievable on the substrate depends also on many other parameters, e.g., the wettability of the surface printed upon and the precision of the positioning system. For successful development of printing processes in the IJP technology, a systematic investigation of the factors influencing the printing result is necessary. For this purpose, it is essential to investigate and control the so-called “Magic Triangle of Inkjet Printing Technology,” which is determined by three main components: the ink, the substrate, and the printhead, as shown in Figure 1a. The systematic

development process includes an analysis of the ink wetting behavior on the individual substrates (better wetting results in a larger droplet diameter, i.e., decreases the printing resolution and image quality, respectively) and studies concerning the adhesion of the dried layer. In particular, the ink system has to be adjusted concerning its rheology with respect to the specifications of the utilized printhead. This procedure requires a continuous adjustment or readjustment of the parameters shown in the “Magic Triangle of Inkjet Printing Technology,” as generally an alteration of one parameter influences all others.^[32] In a typical development procedure, one first formulates the ink according to the specification window of the printhead, as shown in Figure 1c.^[34] The printability of the ink formulation is quantified by the Ohnesorge number Oh, which accounts for rheological ink properties such as density ρ , viscosity η , surface tension σ , and a given nozzle diameter d . Often these parameters are visualized in the dimensionless Reynolds number Re and Weber number We, derived from the Navier–Stokes flow equation

$$\text{Oh} = \frac{\sqrt{\text{We}}}{\text{Re}} = \frac{\eta}{\sqrt{\rho \cdot \sigma \cdot d}} \quad (1)$$

Ohnesorge et al. show that the inverse Ohnesorge number $Z = \text{Oh}^{-1}$ should be between 1 and 10 for optimal printing.^[33] For a typical nozzle diameter of 20 μm , the ink viscosity should be between 1 and 25 mPa s and the surface tension between 25 and 50 mN m^{-1} .^[35–37] To prevent nozzle clogging, the tolerated particle size is in the order of 1% of the orifice diameter. High-boiling-point solvents (T_b beyond 150 °C) or mixtures of such are used to avoid clogging, early drying, and uncontrollable film formation. The droplet forming process as such is optimized by adjusting the voltage wave form of droplet formation and velocity (via printhead parameters like rise time, fall time, pulse width, pulse voltage, printing frequency, printhead temperature, etc.) of the piezo using a drop-watcher system. Here, the viscosity of the ink can be adjusted within a certain range using printhead heating, yet only in a fairly narrow range to avoid unintended ink drying on the nozzle plate. With this in mind, stage/substrate conditioning at elevated temperatures can also have a beneficial influence on the drying behavior of the ink on the target substrate. The wettability of solvents on different substrates, can be quantified by the contact angle formed between a drop of solvent and the solid surface. The contact angle θ depends significantly on the free solid surface energy σ_s , the interfacial energy σ_{sl} , and the solvent surface tension σ_l , and is expressed by the Young's equation, as shown in Figure 1d

$$\sigma_{sl} = \sigma_s - \sigma_l \cdot \cos \theta \quad (2)$$

determine the surface free energy, the contact angle of liquids of different polarity is measured. The aim is to investigate the influence of the changed polarity and thus the changed interaction of wettability and adhesion. Data are evaluated using Owens–Wendt–Rabel and Kaelble (OWRK) method, the surface tension and surface energy are divided into polar and disperse fractions.^[38–40] The disperse fraction describes the temporary fluctuations of the electron density in the molecules. Polar interactions occur in molecules with a permanent dipole moment (e.g., in water due to a different electronegativity of the binding partners and simultaneous asymmetry of the molecule). According to the OWRK method, only interaction between the same phases (disperse or polar) takes place. It follows immediately that only liquids with a similar polar and disperse fraction as the solid (substrate) have a low interfacial energy and thus show good wettability. To evaluate the spreading behavior of a specific solvent on a certain substrate, a wetting envelope in regard to the polar and dispersive part is investigated. In general, solvents within the curve wet the substrate, whereas solvents outside the curve dewet.^[41] A surface treatment or cleaning cycle may change the wetting behavior, as well as storage under different atmospheric conditions, especially in case of transition metal oxide contact layers.^[42]

2.2. Printing Crystallizing Materials

Crystalline MHPs are fabricated from dissolved precursor inks and are subsequently dried from the deposited wet film. In contrast to printing of other electronic or optoelectronic materials, such as metal nanoparticles, metal–organic precursors, or conjugated polymers, in which the drying of the film depends

essentially on solvent evaporation, crystallization in the printing process of MHPs is of utmost importance for functional perovskite thin films and later applications. Apart from the general considerations of IJP summarized in the previous section, processing and printing of MHPs undergo crystallization during solidification, hence require consideration of nucleation and growth processes as shown in Figure 2, as these will significantly affect the coverage and optoelectronic quality of the resulting semiconductor. In this context, it can be assumed that the nucleation of MHP seed crystals in an inkjet-printed droplet follows the classical nucleation theory, proposed by LaMer and Dinegar^[45] with the nucleation rate

$$I \propto \exp\left(\frac{-Q_D}{RT}\right) \exp\left(\frac{-\Delta G^*}{RT}\right) \quad (3)$$

where Q_D is the activation energy for the diffusion of monomers to the nucleation center and ΔG^* is the “nucleation barrier” (activation free energy for nucleation).^[44,46] Nucleation may occur either homogeneously within the droplet with an activation energy of ΔG_{homo}^* or heterogeneously at the droplet/substrate interface with an activation energy of $\Delta G_{\text{hetero}}^*$. The ratio between the two is dependent on the contact angle θ given by Equation (4)

$$\Phi = \frac{\Delta G_{\text{hetero}}^*}{\Delta G_{\text{homo}}^*} = \frac{(2 + \cos \theta)(1 - \cos \theta)^2}{4} \quad (4)$$

Heterogeneous nucleation will therefore dominate at contact angles $< 180^\circ$, which means that crystal growth and thus the morphology of the resulting MHP thin film will be strongly determined by the substrate. While it has been hypothesized that a high density of heterogeneous nuclei should be beneficial for high substrate coverage, the substrate surface morphology might also negatively affect MHP thin-film morphology and coverage.^[44,47]

Apart from nucleation, thin-film formation and morphology is determined by crystal and grain growth. The Johnson–Mehl–Avrami–Kolmogorov (JMAK) model has with some success been utilized to describe isothermal phase transformations in MHP thin-film crystallization.^[48–51] The model describes isothermal growth or phase transition to a target state, γ , as a function of time elapsed, t , and can in its most general form is expressed as

$$\gamma(t) = 1 - \exp(-Kt^n) \quad (5)$$

where K is a kinetic parameter associated with monomer transport to the crystallization center and the growth exponent, n , reflects the nature and dimension of growth.^[52–54] This formalism has successfully been utilized to describe MHP thin-film formation from precursors or intermediate states. In this respect, the growth of MHP thin films via crystalline intermediates containing solvents and/or spectator ions is of utmost importance in determining the quality and morphology.

Altogether, when printing crystallizing materials such as MHPs from dissolved precursors, solvents cannot be considered only to be solubilizing the solvate but may directly influence and be incorporated in precursors and intermediate phases. To control the crystallization conditions and optimize the processing parameters for IJP, the development of inks with

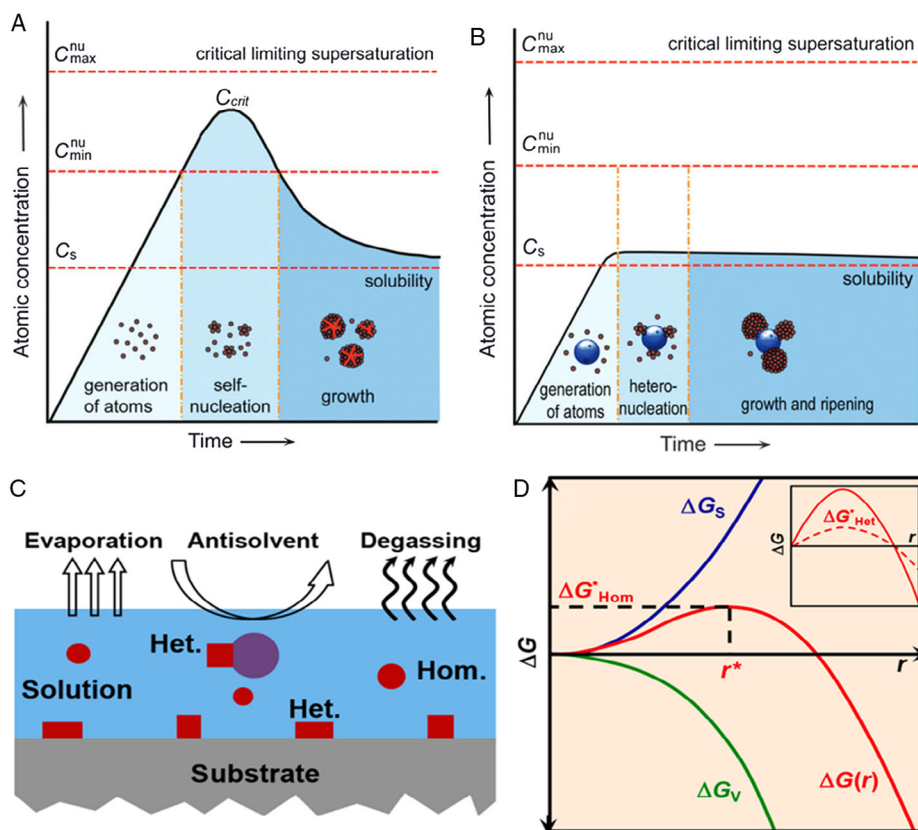


Figure 2. a) LaMer model describing nucleation and growth of nanocrystals as a function of reaction time and concentration of precursor atoms. Reproduced with permission.^[43] Copyright 2013, Royal Society of Chemistry. b) Modified LaMer model describing the formation of hybrid structures through heteronucleation. Reproduced with permission.^[43] Copyright 2013, Royal Society of Chemistry. c) Schematic illustrations of homogeneous and heterogeneous nucleation during super saturation of the thin film. Reproduced with permission.^[44] Copyright 2018, American Chemical Society. d) Change of free energy $\Delta G(r)$ as sum of volume ΔG_v and surface ΔG_s free energy changes as a function of nucleus radius r . Inset for heterogenous nucleation. Reproduced with permission.^[44] Copyright 2018, American Chemical Society.

a sufficiently large process window that allows sample transfer to defined post-treatment conditions could prove advantageous. Recently, key insights into the solution and complex chemistry of MHP precursor solutions and how solvents can positively or negatively affect the thin-film morphology by forming crystalline solvate intermediate phases has been gained, which will be summarized in Section 3.1. Substrate modification providing a favorable surface for homogeneous nucleation is one of the means to optimize printed MHP layer morphology and coverage. Examples will be discussed in Section 3.2. In addition, process control and the utilization of controlled annealing or quenching during or after deposition is of utmost importance when printing MHP layers and will be further discussed in Section 3.3.

3. From Perovskite Ink to Printed Nanocrystals, Wires, and Thin Films

To print MHP semiconductors for photovoltaics, light-emitting diodes, or other optoelectronic applications, different requirements apply with respect to the coverage, morphology, and

optoelectronic quality of the material. For thin-film solar cells, pinhole-free and uniform MHP layers with large grain size and low surface roughness are essential. For lighting and sensing applications, well-defined single crystals with high mobilities and good optical properties are required. IJP is a suitable technique that offers both ways of perovskite fabrication, shown throughout this Review. This section summarizes insight gained into aspects of ink development, crystalline intermediates, substrate modification, and process engineering that are of fundamental importance to devise strategies to control the perovskite crystallization.

3.1. Ink Development

Perovskite precursor solution contains dissolved precursor salts often in aprotic polar solvents. Dissolved precursor salts form ionic complexes or colloids, that can be considered “building blocks” of the semiconductor formed upon solvent removal and solidification. Hence these affect the perovskite crystallization dynamics and resulting thin-film morphology. A good control over the ink properties is therefore necessary to reproducibly manufacture high-quality thin films. As shown in Figure 1,

mainly the solvents used with regard to concentration, viscosity, surface tension, and flow dynamics determines the process window of IJP as a deposition method. In general, high-boiling-point and low-vapor-pressure solvents are beneficial to prevent nozzle clogging and early crystallization of the precursor ink. Apart from solubilizing precursors, solvents may also actively affect the molecular structure of precursor complexes, as further discussed in Section 3.1.1., and become incorporated into crystalline intermediate phases that may affect the resulting thin-film morphology. Likewise, the precursor composition and ratio determine the formation of intermediate phases that may influence thin-film formation kinetics and microstructure further discussed in Section 3.1.2. Solvent additives are often used in IJP to adjust viscosity and drop shape or to improve film wetting to modulate perovskite nucleation and growth. These additives affect also optoelectronic properties as well as ink stability. Additives, like polymers or other organic molecules, excess organo-metal halide salts, acids, or solvents are widely used in the developed and tested inks and are summarized in Section 3.1.3.

3.1.1. Solvents for Perovskite Inks

In inks for printing MHPs, solvents are more than just solubilizing agents. Apart from parameters pertaining to an ink's printing behavior, solvents determine precursor solubility of precursors, the molecular structure of lead-halide complexes by coordinating to lead and the drying behavior through their boiling point.^[55–57] For commonly used Lewis base solvents such as dimethylformamide (DMF), dimethylsulfoxide (DMSO), gamma-butyrolactone (GBL), *N*-methyl-2-pyrrolidone (NMP), and acetonitrile (MeCN), the solubility of lead halide salts is typically on the order of 1 M.^[58–63] The stronger the Lewis base, the greater the coordination of the solvent-lead adduct.^[60,61] Hansen solubility parameters have been successfully used to rationalize solubility trends of MHP precursors in various solvents, yet they do not account for specific solvent interactions with lead-halide precursor complexes in solution.^[64] The solute-solvent interaction might be more correctly captured by Gutmann's Donor numbers as suggested by Babaei et al. and Hamill et al.^[65,66] In precursor solutions, containing all building blocks of MHPs, solvents may hence compete with halides for coordination to lead.^[67] The precursor complexes and colloids formed in solution constitute the “building blocks” of MHP semiconductors. The importance of solvent participation and competition with metal-halide bonds not only pertains to solutions. Solvents may also become incorporated in crystalline intermediate states. The existence of solvate phases in thin-film formation and their detrimental or beneficial effect on thin-film morphology was recognized early.^[68] The specific crystal structure of intermediate phases of PbI₂-solvent complexes (PbI₂-DMSO, PbI₂-DMF, PbI₂-NMP^[69]) has been identified as well as intermediate crystalline phases also incorporating the monovalent counter ion (e.g., [(MA)₃PbI₅·2DMSO]_n). These affect the morphology of crystalline intermediate phases that may persist even upon solvent removal, defining the morphology of thin films. The effect of differences in solvent coordination strength and formation of various intermediate structure can be observed in a study by Liu et al., who investigated pure and mixtures of

GBL and DMF as solvents in MHP inks to fabricate inkjet-printed MHP thin films (see **Figure 3a**).^[70] Pure GBL causes formation of island-shaped polycrystalline perovskite domains, whereas DMF results in isotropic growth of dendritic and nanowire structures, more than 30 μm in length, consistent with results of previous works.^[74,75] A mixture of GBL and DMF form more uniform crystal plates, but no uniform thin film is obtained. The absence of nanowires is attributed to the faster evaporation of DMF, leading to a GBL-similar drying behavior. In contrast, high coordinating solvents such as DMSO are necessary for homogeneous and pinhole-free thin films. Burgues-Ceballos et al. investigated the influence of several solvents on film morphology of MHP thin films.^[76] Despite positive influence from three high-boiling-point solvents, DMSO, γ -valerolactone, and benzaldehyde (compared with DMF main solvent), no significant correlation between the perovskite film morphology with polarity or vapor pressure of the tested inks were found. Nevertheless, the mildly reducing character of benzaldehyde cause an homogeneous morphology and optical dense layers by preventing oxidation of unstable precursor solution and reduction of oxidized constituents.^[76] The results suggest that the perovskite crystallite morphology relies heavily on the solvent used for preparation of the inks. Mixtures of solvents where single components fulfill different purposes become more and more important. The designed ink has to ensure precursor solubility, beneficially coordinating states in the solution, whereas the other components fulfill the purpose of controlling ink properties of relevance for printing such as viscosity and fluid dynamics. Wang et al. could show that a mixture of DMSO/2-methylpyrazine/1-propanol provides uniform thin films and highly efficient solar cells.^[77] When printing MHP thin films, especially when scaling technologies to industrial production, it is necessary to find nontoxic solvent systems.^[64,65] Gardner et al. found a general trend that γ -butyrolactone/alcohol/acetic acid results in homogenous film formation, attributed to the mixture of low- and high-boiling-point solvents.^[64]

3.1.2. Perovskite Precursor Composition

Fascinatingly, MHPs have been found to form crystalline ABX₃ perovskite structures from a large variety of precursors. Changing the stoichiometry between the MAI and PbI₂ precursors affects the morphology and/or stability of the resultant film.^[78] Additional methylammonium chloride or bromide act as counter ions in the precursor solution. This strategy is referred to “spectator ion” process as bromide or chloride may intermittently be incorporated, hence change crystallization kinetics but evaporate during annealing.^[51,72,79] In addition, bromide and chloride exhibits a stronger coordination to lead compared to iodide, affecting the solution complex chemistry.^[41,59,71] Hence, spectator ions might act as seed crystals, suppressing solvate intermediates and the direct formation of ABX₃ crystals.^[80–82] With respect to IJP, this will be beneficial as a broader process window is expected enabling the separation of printing and annealing process steps. Yang et al. reported that excess of MAI results in a highly crystalline film independently of the annealing time between 1 and 15 min.^[59] Li et al. found a

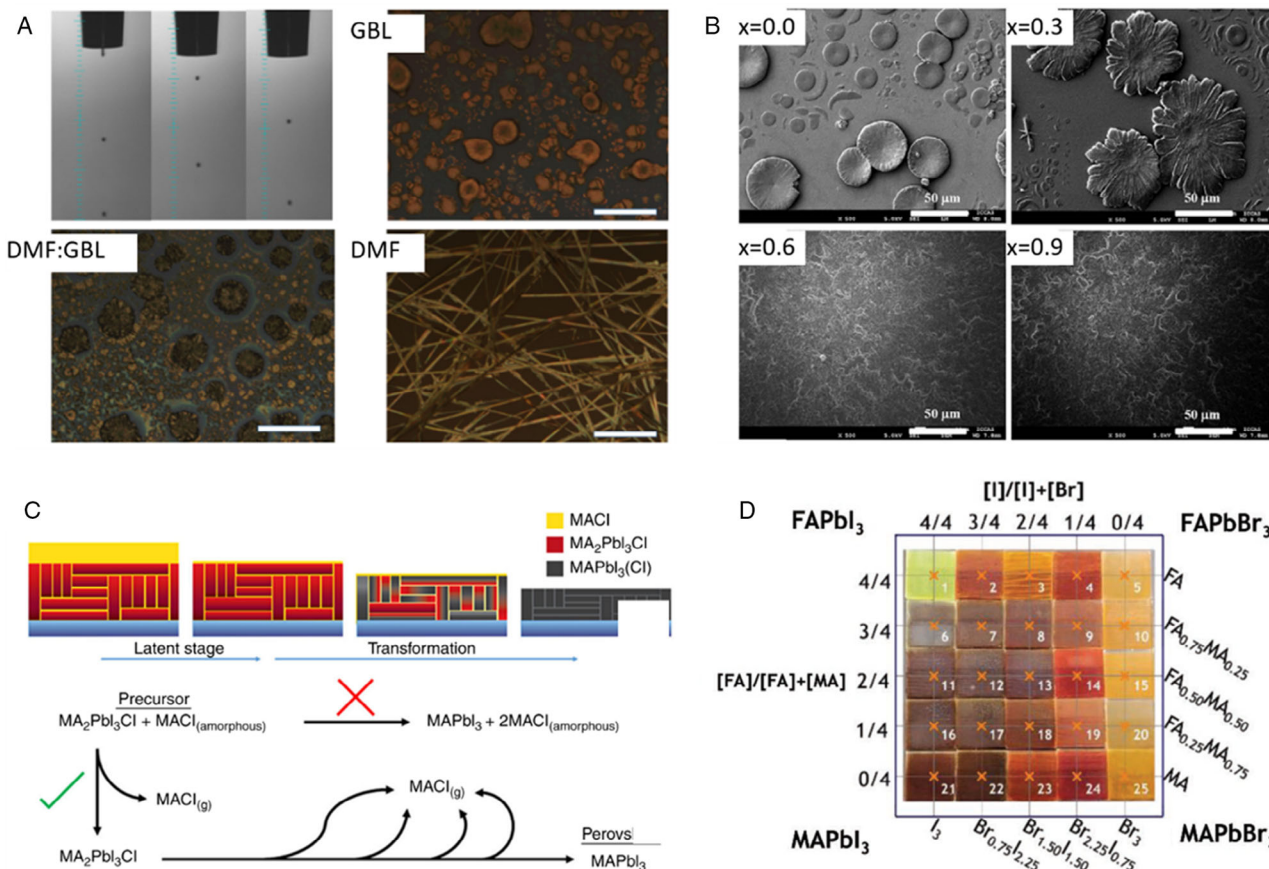


Figure 3. a) Effects of solvent on the crystallization of inkjet-printed layers. Scale bar 10 μm. Adapted with permission.^[70] Copyright 2017, American Chemical Society. b) Influence of spectator ion (MACl) on inkjet-printed MAPbI₃ layers. $x = 0$, $x = 0.3$, $x = 0.6$, and $x = 0.9$ (for ratio 1 - x :1: x of PbI₂:MAI:MACl). Reproduced with permission.^[71] Copyright 2015, Royal Society of Chemistry. c) Self-regulating and chemical model of the transformation from precursor to perovskite. Reproduced with permission.^[72] Copyright 2014, American Chemical Society. d) Four-channel combinatorial inkjet-printed perovskite layers. Adapted with permission.^[73] Copyright 2019, Wiley-VCH.

beneficial impact of MACl in a MAPbI₃ precursor solution, when inkjet-printed on a mesoporous TiO₂ scaffold.^[71] Both morphology and absorption of MHP thin films improved with the addition of 60 wt% of MACl (see Figure 3b). In addition, Gheno et al. reported on the positive influence of MACl regarding the wetting of the MHP ink on an electron transport layer of TiO₂. The better control of perovskite formation results in an improved interfacial coupling between the lead *p* and the titanium *d* conduction band states, enhancing charge carrier extraction.^[41,83] The results indicate that the spectator ions control the crystallization process and thus the morphology during the formation of the perovskite, to fabricate uniform and dense MHP layers (see Figure 3c). In addition, multication and multianion ABX₃ perovskites are investigated for fine tuning the bandgap and improving stability. Alkanes, such as cesium^[84–87] and rubidium,^[88–90] added in small amounts (1–20 wt% with respect to all cations) stabilizes the ABX₃ crystal structure and reduces the trap density. Organic halide compounds with larger ion radii effecting both the preferred crystal phase as well temperature and moisture stability.^[91] These materials can be time-effectively explored by combinatorial multichannel printing as demonstrated by

Bag et al., who found that a MAI-to-FAI ratio of 2:1 results to uniform film morphology for inkjet-printed perovskite thin films, compared with pure MAPbI₃ or FAPbI₃ films.^[92] Recently, Chen et al. showed rapid screening of MHPs, utilizing four-channel IJP.^[73] The high-throughput approach was used to screen mixtures of four inks containing defined mixtures of MA, FA, I, and Br, as shown in Figure 3d. In addition to FA/MA mixtures,^[92,93] other organic halides such as 2-phenylethylammonium (PEA)^[94] or guanidinium^[95] were investigated with beneficial influence on morphology, crystallization, and stabilization of the black MHP phase. Interestingly, precursors containing hydrated form of PbOAc cause the formation of highly crystalline solvent-free intermediate phases, hence the formation of pillar-like grains with lateral dimension of several tens of micrometers.^[96–98]

3.1.3. Precursor Additives

Of particular importance for printing are additives that change the ink properties, especially viscosity, surface tension, and

wetting behavior, which can be adjusted by liquid surfactants or polymers.^[42,99] Moreover, additives change the solution chemistry, the formation of complexes and colloids and thus influence the crystallization and quality of the final MHP layer. Small amounts of additives were found to have a beneficial effect on the crystallization kinetics, thereby improving grain size, layer uniformity, and defect density. It has been reported, that inorganic acid additives modify crystallization dynamics via different mechanisms. For hypophosphorous acid (HPA), PbHPO_3 colloids are forming in a reaction cascade of HPA with HI, MA, and PbX_3 , which act as nucleation centers in the perovskite ink.^[100–103] A similar behavior is found for 5-ammoniumvaleric acid (5-AVA), forming a template structure for the perovskite growth.^[104] On the contrary, hydrohalic acids such as HI, HBr, and HCl increase the solubility of dissolved lead(II) species,^[105] thereby triggering the dissolution of plumbate colloids.^[106] The increased concentration of super saturation and the lower colloid concentration slow down nucleation and crystal growth, resulting in smooth perovskite layers with large grains.^[105–108] Salts such as NH_4Cl slowly decompose into NH_3 and HCl at ambient conditions. This ensures the formation of MHP during processing, even in absence of additional thermal annealing.^[109,110] Alkali salts such as sodium iodide and chloride (NaI and NaCl) as well as potassium chloride, iodide, and nitrate (KI, KCl, and KNO_3) added as interface modifiers are proven to suppress hole trapping at the n-type selective transport layer/perovskite interface.^[111,112] Incorporated liquid additives such as diiodooctane (DIO) or 1-chloronaphthalene facilitate homogenous nucleation and modulate the kinetics of growth during crystallization.^[113,114]

Giuri et al. tuned the rheological parameters of the ink, by adding corn starch to a MAPbI_3 precursor.^[115,116] The surface tension and viscosity values are tuned for optimal printing conditions from 43 to 53 mN m^{-1} and from 2 to 8 mPa s , respectively. The starch biopolymer establishes a hydrogen interaction with MAI, leading to compact and homogenous films. The starch network gives the perovskite film a higher resistance to bending stress, enabling flexible perovskite-based applications. In addition, the hygroscopic nature of starch stabilizes the perovskite from humidity degradation.

3.2. Substrate Sensitivity

In addition to the ink also the substrate strongly affects printing results. Especially the wetting or contact angle of droplets on the substrate surface, a measure of surface energy has to be considered, when printing functional materials. For a given perovskite precursor ink, surface roughness, temperature, and adhesion force change the wettability, hence the crystallization of the MHP.

3.2.1. Substrate Temperature

The substrate temperature has two main effects: a) improving the wetting, by lowering the surface energy of the substrate and b) increasing the rate of solvent evaporation, affecting the crystallization. The influence of substrate temperature on ink-jet-printed MHP thin-film morphology was discussed by

Liu et al. who investigated equimolar MAI and PbI_2 precursor inks in mixed DMF:GBL solutions.^[70] MHP samples were printed at different temperatures ranging from 25 to 75 °C and annealed in a N_2 -filled glovebox. Lower temperatures favors the formation of nano- or microdendritic networks, due to presence of solvate intermediate phases, whereas island growth is observed at higher temperatures. This reflects that the process temperature and associated evaporation rate affects the crystallization kinetics and hence coverage and microstructure of the resulting MHP thin films. The study also cautions that elevated processing temperatures may result in clogging of printhead nozzles due to the evaporation of the solvent at the orifice.

To obtain defined MAPbBr_3 single crystals by IJP, Gu et al. cooled low adhesion Si substrates down to 5 °C.^[117] Different sizes of perovskite single crystals of $d = 3.2, 6.7, 11.3,$ and $17.2 \mu\text{m}$ were achieved by controlling the inkjet droplet volume from 1, 10, and 30 to 60 pL. The crystal shape and microstructure was strongly dependent on the substrate surface polarity/functionalization/energy, further discussed in the next section, as well as the substrate temperature. This is mainly due to the increasing evaporation rate of the droplet with increasing temperature.^[118,119] At low temperature (below 5 °C), the Marangoni convection within the droplet is weak, causing a low nucleation rate,^[120] and results in single crystal formation. The gas–solution interface (pinning, surface tension) is believed to have a massive influence on the crystal shape. At higher temperatures above 15 °C, the rapid evaporation of the solution results in uncontrollable supersaturation and higher nucleation rate and multiple dome-like crystals form, due to the faster solvent evaporation. Li et al. printed a MAI and PbI_2 containing precursor ink from GBL-solution on a mesoporous TiO_2 substrate and studied the influence of in situ substrate temperature to the later perovskite film morphology.^[71] At room temperature, various shapes of perovskite crystallites (islands) are visible from scanning electron microscopy images. Increasing the temperature improves substrate coverage and crystallite growth, with an optimum at a substrate temperature of 50 °C. Further increasing the substrate temperature results in formation of pinholes. The variation of crystallite size and film coverage can be attributed to the solvent evaporation rate, which results to self-assembling at low temperatures and the formation of islands and fast evaporation at high temperatures. The results indicate that monitoring the process temperature during the printing process to determine the ideal temperature range is of great importance to control the film morphology of different inks and substrates.

3.2.2. Substrate Adhesion and Wetting

In addition to substrate temperature, the wetting of the printed ink drops to the surface can be tuned, by controlling the adhesion, measured by the drop contact angle. Gu et al. demonstrated, that the crystallite structure and wetting of the printed ink directly depends on the surface adhesion force, by manipulating the contact line.^[117] On high adhesion substrates, e.g., good wetting, the nucleation free energy is lowered and heterogeneous nucleation, as described in Section 2.2., starts from multiple seed crystals within the deposited droplet.^[121,122] The outward capillary flow causes an gathering of the perovskite

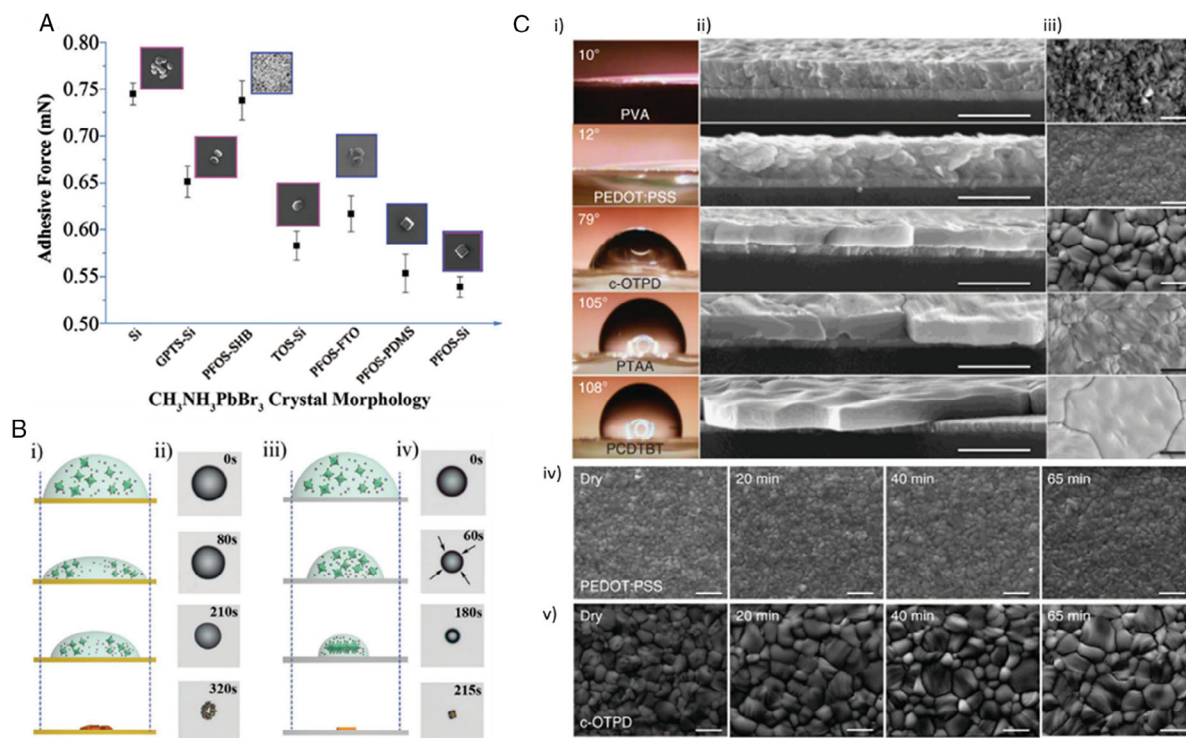


Figure 4. a) Change of MAPbBr₃ crystals on substrates with varying adhesion forces/wetting. Reproduced with permission.^[117] Copyright 2017, Wiley-VCH. b) Perovskite crystallization on (i), (ii) high adhesion and (iii), (iv) low adhesion substrate. Reproduced with permission.^[117] Copyright 2017, Wiley-VCH. c) MAPbI₃ films grown on wetting and nonwetting HTLs: i) contact angle, ii) SEM cross section and iii) top view: iv) and v) after drying at 105 °C. Scale bar 1 μm. Adapted with permission.^[123] Copyright 2015, Nature Publishing Group.

molecules within the droplet edges, where nucleates are formed, hence support the formation of polycrystalline samples (see **Figure 4a,b**). The roughness of the substrate may also increase the nucleation number.^[120] On a low adhesion substrate, a receding of the printed droplet is visible during the evaporation of solvent. Due to the fast retraction or depinning of the contact line, the perovskite molecules inside of the droplets gather and form single crystals with a regular shape, as described as homogeneous nucleation in Section 2.2. Bi et al. demonstrated high aspect ratio crystalline perovskite grains on nonwetting surfaces, as shown in **Figure 4c**.^[123] In this attempt, the crystal growth is influenced by thermal annealing, which drive the interdiffusion to form perovskite grains. Grain boundaries were pinned, most likely, by the impurities lying at the grain boundaries. On high wetting films, induced by hydroxyl groups from poly(3,4-ethylenedioxythiophene):poly(styrenesulfonate) (PEDOT:PSS) or polyvinyl alcohol (PVA) small MHP grains below the film thickness are formed by heterogeneous nucleation and a large number of nuclei. In contrast, highly hydrophobic, nonwetting substrates such as poly(bis(4-phenyl)(2,4,6-trimethylphenyl)amine) (PTAA) and poly(*N*-90-heptadecanyl-2,7-carbazole-alt-5,5-(40,70-di-2-thienyl-20,10,30-benzothiadiazole)) (PCDTBT) result in large grains with an average grain size of 1 and 7.9 times the film thickness, because the nuclei density is decreases leading to a suppressed heterogeneous nucleation. Most of the grain boundaries are perpendicular to the nonwetting substrates, minimizing the grain boundary energy. The result of low-defect density and

high-quality perovskite polycrystalline thin films, show better optoelectronic properties such as fewer bulk and surface traps, and higher charge carrier mobilities, which makes them interesting for transistors (high μ), photodetectors (low charge traps), and lighting applications. The wetting of hydrophobic surfaces can be tuned, by plasma treatment, shown by Zhang et al.^[124] Short O₂ plasma on top of PTAA destroys the upper hydroxyl layers open up the possibilities of the ionic perovskite ink to wet. Another, non-destructive process was shown by Schultes et al.^[125] A thin layer of Al₂O₃ or SiO₂ nanoparticles on top of the surface contact layer, shows beneficial wetting to the ionic perovskite ink. Li et al. obtained a two-step IJP process on mesoporous substrates which guarantee fast and complete coalescence of the precursor droplets and limit random diffusion of the precursor solution, due to capillary effects.^[126] Mesoporous TiO₂ serves as an ultrahydrophilic low free energy surface and the printed PbI₂ droplets coalesce to uniform liquid membrane and the solute diffuse into the mesoporous layer. The overall objective is to print on a good wetting substrate, which allows to control crystallization from a homogeneous nucleation at the air-solution interface through rapid supersaturation induced by gas or solvent quenching processes described in the following section.

3.3. Process Engineering

As apparent from previous sections, controlling the nucleation and crystallization of MHP is of crucial importance to obtain

high quality layers. As shown in Section 3.1 and 3.2, the composition of the precursors ink as well as substrate properties affects crystallization and thin-film microstructure. In addition, various methods have been developed to control MHP film formation.

3.3.1. Solvent Removal

Printing MHP from precursors in high-boiling-point solvents in a one-step process results in thick wet films directly after printing and enlarged processing windows (see **Figure 5a**). To induce crystallization, solvent has to be removed. One of the most utilized strategies for spin coating is the deposition of antisolvents (toluene, chlorobenzene, and ethylacetate) during spinning.^[68,129,130] Antisolvents either remove some of the MHP ink solvents or are mixed into the wet film causing oversaturation. Seed crystals are formed preferentially on top of the MHP layer where the crystallization is induced.^[123] This strategy is however impractical to be used in an IJP process.^[70] Nevertheless, the remaining challenge for IJP is to induce fast nucleation, whereas the crystal growth is delayed to form

pinhole-free and oriented MHP layers. Alternative strategies to achieve controlled crystallization via IJP were investigated, including temperature,^[70,117,118,131] gas quenching,^[132–137] and vacuum-assisted^[127,138,139] solvent removal, shown in **Figure 5b**.

3.3.2. Two-Step Conversion

Due to the different solvent-dependent solubility of lead and halide compounds, the deposition of MHP layers in two consecutive steps is advantageous for process control, e.g., grain size, film coverage, and reproducibility.^[140] Controlling the heterogeneous nucleation rate to control later film coverage and morphology is of utmost importance. Therefore, the crystallization depends on the interaction of the two precursor components on the substrate and can be controlled by the morphology of the PbI_2 layer, deposited first.^[141,142] High optical density MHP thin layers were obtained by spin coating of PbI_2 and MAI sequentially on a mesoporous TiO_2 scaffold. Here, the mesoporous layer enhances the heterogeneous nucleation rate, thus increasing the film coverage. At high MAI concentrations,

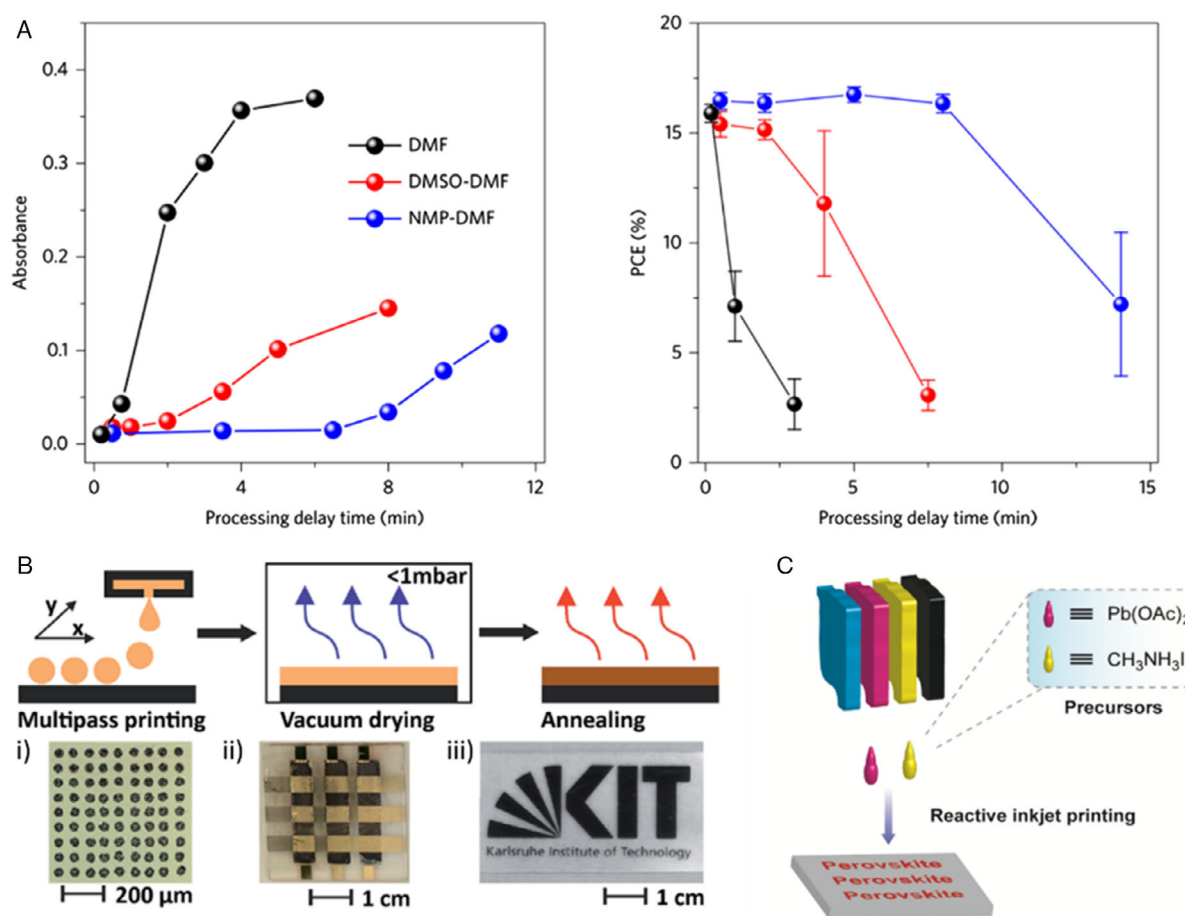


Figure 5. a) Utilization of high-boiling-point solvents allows to separate the printing and drying processes (seconds to minutes). Reproduced with permission.^[59] Copyright 2017, Springer Nature. b) Multipass printing approach of one-step MAPbI_3 ink with additional vacuum drying step, to extract excess solvents and form uniform perovskite layers. Reproduced with permission.^[127] Copyright 2016, Royal Society of Chemistry. c) Schematic of a reactive/combinatorial printing process from two precursor inks, which react wet-in-wet on the surface. Reproduced with permission.^[128] Copyright 2016, The Authors.

a direct conversion is observed and MAI diffuses through the PbI_2 structure and pillar-like grains, perpendicular to the substrate are observed.^[143] In contrast, perovskite crystals being parallel to the substrate are formed^[144] by a dissolution or recrystallization process of additional MAI promoting a dissolution of PbI_2 or MAPbI_3 crystals.^[145] Numerous variations have been described in literature for inkjet-printed two-step processes: a) Printing of MAI or FAI on top of evaporated^[100] or spin-coated^[92,146] PbI_2 , b) Printing of PbI_2 and dipping in MAI solution^[147] or MAI vapor^[126] and c) Printing of PbOAc and MAI, shown in Figure 5c.^[128] Details of these procedures are discussed in Section 4.1. It has been shown that it is advantageous to use strongly coordinating Lewis base solvents such as DMSO and NMP for PbI_2 deposition, as this results in PbI_2 -solvent adducts that can be converted into perovskites by intramolecular exchange when exposed to the monovalent cation, forming large uniform crystals in the process.^[55,69,148–150] For IJP, the results suggest that a two-step conversion process is most suitable on mesoporous contact layers, as this improves pore-filling and surface coverage.^[140] Moreover, compared with a one-step process, the two-step process seems to be more forgiving, when fabricated at ambient and humid conditions.^[151]

3.3.3. Local Modification of Properties by IJP

IJP offers the possibility of structured and defined deposition of ink on certain substrates within the micrometer resolution. This major advantage over other printing and coating techniques offers the possibility to locally tune the perovskite crystal and morphological structure. As an example, Wong et al. tuned the luminescent of CsPbBr_3 perovskite nanocrystals from green to blue and red by printing halide alkanes (*tert*-butyl chloride or *tert*-butyl iodide) on top of nanocrystals and inducing halide exchange through a light-mediated exchange reaction.^[152] Even protection of confidential information printed with CsPbX_3 quantum dots (QDs) is possible, which was shown by Sun et al.^[153] After printing the CsPbX_3 QD, the information is encrypted and decrypted by deposition of butylamine and acetic acid, respectively. During this process, the crystal structure undergoes a change from 3D (CsPbX_3) to 0D (Cs_4PbX_6) perovskite, where 80% of initial photoluminescence is restored after five cycles of decryption and encryption.

4. Inkjet-Printed Perovskite-based Optoelectronics

4.1. Inkjet-Printed PSCs

Different approaches have been developed to achieve highly efficient inkjet-printed PSCs. Both one-step and two-step processes previously developed for spin coating were successfully adapted for IJP which will be detailed in the following sections. In terms of device architectures, printing on mesoscopic metal oxide selective contact layers may prove beneficial for fully printed and low-cost photovoltaics. Table 1 shows inkjet-printed photovoltaic devices distinguishing one-step from two-step deposition methods and device architecture, which are also shown in Figure 6a.

4.1.1. Two-Step Strategy

Wei et al. published the first example of using IJP for PSC manufacturing using a sequential 2-step approach.^[146] The MAPbI_3 perovskite layer is fabricated by first spin-coating of a thin PbI_2 layer on top of a compact TiO_2 layer followed by printing of a carbon containing MAI ink, whereas the carbon serves both as a hole-extraction layer and counter electrode in the bilayer solar cell. After an annealing step at 100 °C, a PCE of 11.6% was obtained from $J-V$ measurement. Further investigations were done by Abzieher et al. utilizing a two-step process, where a thin layer of PbI_2 was evaporated first, which converts to MAPbI_3 after printing a self-made ink containing MAI.^[100] For better printability, a mixture of 2-propanol (IPA) and the high-boiling-point solvent cyclohexanol was utilized. To improve grain size, layer morphology, and crystallization dynamics, hypophosphorous acid (HPA) was added to induce a faster crystallization and a PCE of 6.8% could be achieved. An s-shaped behavior in the $J-V$ -characteristics, limited the PCE was attributed to an incomplete conversion of MAI and PbI_2 and the residual PbI_2 , acting as a charge carrier barrier on top of the c- TiO_2 layer. Li et al. obtained a two-step IJP process on mesoporous substrates that results in fast and complete coalescence of the precursor droplets, and limit random diffusion of the precursor solution.^[126] After printing PbI_2 onto a mesoporous TiO_2 scaffold, MA vapor was used to form uniform and large grain size containing perovskite films. Aspect ratio of grain size to film thickness exceeds five for printed layers, compared with one for PbI_2 spin-coated devices. Grain boundaries are perpendicular to the printed film and to minimize the grain boundary energy. A maximum PCE of 18.64% was achieved for printed devices compared with 16.22% for spin-coated devices on an active area of 0.04 cm². Extracted PL decay times confirmed the facilitated electron extraction and transport from the printed perovskite layer to the mesoporous TiO_2 layer. The printed layers exhibit increasing grain sizes, thus open circuit current density (J_{SC}), open circuit voltage (V_{OC}), and fill factor (FF) were enhanced. High uniformity of the perovskite layer from printed PbI_2 is obtained, when increasing the device area from 0.04 to 2.02 cm², which enables an area-independent PCE of 18.6 and 17.7%, respectively. Spin-coated devices show a drastic area dependency, and PCE drops from 16.22 to only 13.53%, as shown in Figure 6b.

Bag et al. used a multichannel desktop inkjet printer to print different ratios of MAI and FAI on top of a spin-coated PbI_2 film.^[92] The use of a multichannel printheads gives the possibility of in situ mixing and combinatorial screening of different reagents and is, compared with single channel approach, only limited to the physical number of ink cartridges. The composition of the printed layer can be easily and rapidly tuned by varying mixing of separate inks in the multichannel printhead. Utilizing two channels (MAI and FAI) allows for higher reproducibility, due to the printing of different mixtures on a single substrate. The MA-only device crystallizes in the tetragonal phase, whereas the FA-only devices crystallize in the yellow hexagonal nonperovskite phase. The combinatorial approach ensures optimized layer quality when mixing MA to FA in a ratio of 2:1, leading to a maximum PCE of 11.1% for p-i-n device structure on ITO/PEDOT:PSS. Similar to these results, Jiang et al.

Table 1. Summary of inkjet-printed perovskite solar cells, fabricated in various processing techniques and architectures on rigid glass substrates. Perovskite layers are printed at ambient conditions. Printed layers in bold. PCE values extracted from *J*-*V*-characteristics (stabilized power output values in parentheses). VA: vacuum annealing; TA: temperature annealing; VTA: vacuum-assisted temperature annealing; SA: solvent annealing.

	Architecture	Solvent system [vol%]	Annealing	Year	PCE [%]	Area [cm ²]	Ref.
1-step bilayer	FTO/c-TiO ₂ /MAPbI ₃ /Spiro-MeOTAD/Au	DMSO:GBL (7:3)	VA and TA	2016	11.3	0.09	[127]
	ITO/PEDOT:PSS/PbOAc+MAI/PCBM/Ca/Al ^{a)}	Water:IPA	TA	2016	0.93	n.a.	[128]
	FTO/c-TiO ₂ /Cs _{0.1} (MA _{0.17} FA _{0.83}) _{0.9} Pb(Br _{0.17} I _{0.83}) ₃ /Spiro-MeOTAD/Au	DMSO:DMF:GBL (1:4:5)	VA and TA	2018	15.3 (12.9)	0.09	[154]
	FTO/c-TiO ₂ /Cs _{0.1} (MA _{0.17} FA _{0.83}) _{0.9} Pb(Br _{0.17} I _{0.83}) ₃ /Spiro-MeOTAD/Au	DMSO:DMF:GBL (1:4:5)	VA and TA	2018	11.5	0.024	[155]
	FTO/c-TiO ₂ /C ₆₀ /MAPbI ₃ /Spiro-MeOTAD/Au	DMSO:GBL (4:6)	VTA	2018	17.0 (16.6)	0.4	[139]
	FTO/c-TiO ₂ /C ₆₀ /MAPbI ₃ /Spiro-MeOTAD/Au	DMSO:GBL (4:6)	VTA	2018	13.3	4.0	[139]
	ITO/WO ₃ /MAPbI _{3-x} Cl _x /Spiro-MeOTAD/Au	DMF+ 1 wt% DIO	TA	2018	10.7	n.a.	[41]
	ITO/NiO _x /Cs _{0.1} (MA _{0.17} FA _{0.83}) _{0.9} Pb(Br _{0.15} I _{0.85}) ₃ /C ₆₀ /Au	DMSO:DMF:GBL (26:30:44)	VA and TA	2019	20.7 (18.5)	0.105	[156]
	ITO/PEDOT:PSS/FA _{0.75} MA _{0.25} PbBr _{0.75} I _{2.25} /PCBM/BCP/Ag ^{a)}	DMF:DMSO (4:1)	TA	2019	7.31	n.a.	[73]
	ITO/PEDOT:PSS/MAPbBr _{0.75} I _{2.25} /PCBM/BCP/Ag ^{a)}	DMF:DMSO (4:1)	TA	2019	9.48	n.a.	[73]
1-step mp	FTO/c-TiO ₂ /mp-TiO ₂ /MAPbI _{3-x} Cl _x /Spiro-MeOTAD/Au	GBL	n.a.	2015	12.3	0.04	[71]
	FTO/c-TiO ₂ /mp-TiO ₂ /mp-ZrO ₂ /Carbon-paste/MAPbI ₃ -5-AVA	GBL	TA	2016	9.5	0.16	[157]
	FTO/c-TiO ₂ /mp-TiO ₂ /mp-ZrO ₂ /Carbon-paste/MAPbI ₃ -5-AVA	GBL	TA	2017	8.6	0.16	[158]
	FTO/c-TiO ₂ /mp-TiO ₂ /MAPbI _{3-x} Cl _x /Spiro-MeOTAD/Au	DMF	TA	2019	<1	n.a.	[159]
	FTO/mp-TiO ₂ /Cs _{0.1} Gua _{0.05} FA _{0.83} MA _{0.17} PbI _{2.63} Br _{0.37} /Spiro-MeOTAD/Au	DMF:DMSO:GBL:NMP (33:28:33:5)	SA ^{b)} and TA	2019	14.1 (12.0)	0.064	[160]
2-step bilayer	FTO/c-TiO ₂ /PbI ₂ /MAI+C	IPA	TA	2014	12.0	0.15	[146]
	ITO/PEDOT:PSS/PbI ₂ /(FAI) ₂ :MAI/PCBM/Ca/Al ^{a)}	IPA	TA	2015	11.0	n.a.	[92]
	ITO/PEDOT:PSS/MAI+PbI ₂ /PCBM/Ca/Al	DMF (PbI ₂), IPA (MAI)	TA	2016	3.73	n.a.	[128]
	ITO/c-TiO ₂ /PbI ₂ +MAI/Spiro-MeOTAD/Au	IPA:Cyclohexanol:HPA	TA	2017	8.0	0.09	[100]
2-step mp	FTO/mp-TiO ₂ /PbI ₂ +MAI/Spiro-MeOTAD/Au	DMF:DMSO	TA	2018	18.6 (18.3)	0.04	[126]
	FTO/mp-TiO ₂ /PbI ₂ +MAI/Spiro-MeOTAD/Au	DMF:DMSO	TA	2018	17.7	2.02	[126]

^{a)}Indicate devices processed by wet-in-wet combinatorial approach; ^{b)}Immersed in diethyl ether.

demonstrated the use of a multichannel inkjet printer to separately deposit lead(II) acetate trihydrate [Pb(OAc)₂·3H₂O] and MAI on the same spot of solid substrates.^[128] An aqueous solution (water and IPA in 1:1 ratio) is mixed in 3:1 ratio (MAI to PbOAc) on PEDOT:PSS, as shown in Figure 6c. A relatively low efficiency of 1% was observed due to very thin and non-uniform perovskite layer with wire-like crystallites. Furthermore, PEDOT:PSS is partially dissolved by aqueous inks and is affected during reactive Inkjet process. Nevertheless, these results are showing the great potential of combinatorial in situ printing.

4.1.2. One-Step IJP

The one-step approach is a quite common method to achieve high-efficiency PSCs. Hereby, the printed precursor solution contains all the compounds to crystallize in the perovskite structure. Li et al. inkjet printed the first MAPbI₃ perovskite ink on a mesoporous TiO₂ film.^[71] Devices show a PCE of 7.9%, when printed from a MAPbI₃-GBL ink on a heated substrate (50 °C). The addition of spectator ion, e.g., MAcl (60%) influences the crystal growth leading to an increase in PCE to 12.3%, extracted from *J*-*V* characteristics. The main effect of the added MAcl is in the improved morphology and thick and uniform perovskite layer, leading to an enhanced absorbance in the visible

wavelength region (500–800 nm). Mathies et al. show for the first time, a one-step printing process of MAPbI₃ on top of a compact TiO₂ layer.^[127] They use a multipass printing approach where they adjusted the film thickness by printing several perovskite layers on top of each other. In addition, the multilayer approach results in an increase in grain size, due to recrystallization by redissolving already printed layers. To obtain crystalline, pinhole-free, and smooth perovskite layers, Mathies et al. introduced a vacuum annealing step providing a faster solvent extraction and prevention of the intermediate MAI–DMSO–PbI₂ perovskite layer. Highly uniform and flat layers were printed which result in a PCE of 11.3% close to the spin-coated reference devices of 12.8%. Liang et al. adapted the vacuum annealing post process, by a vacuum-assisted thermal annealing (VTA) to further improve the PCE of printed PSCs.^[139] Annealing at 90 °C at a pressure of 50 Pa provides optimal conditions to form crystalline and uniform MAPbI₃ layers and a PCE of 14%. By adding a thin layer of C₆₀ on top of the hydrophilic TiO₂ layer, the PCE increases to 17.04% with negligible hysteresis. The increase in PCE is mainly attributed to larger grain sizes of the MAPbI₃ on TiO₂/C₆₀ substrates compared with pure TiO₂ layers. The lower wettability of the substrate effectively inhibit heterogeneous nucleation, and result in less dense nuclei and larger grain size. Increasing the C₆₀ thickness above 10 nm causes poor

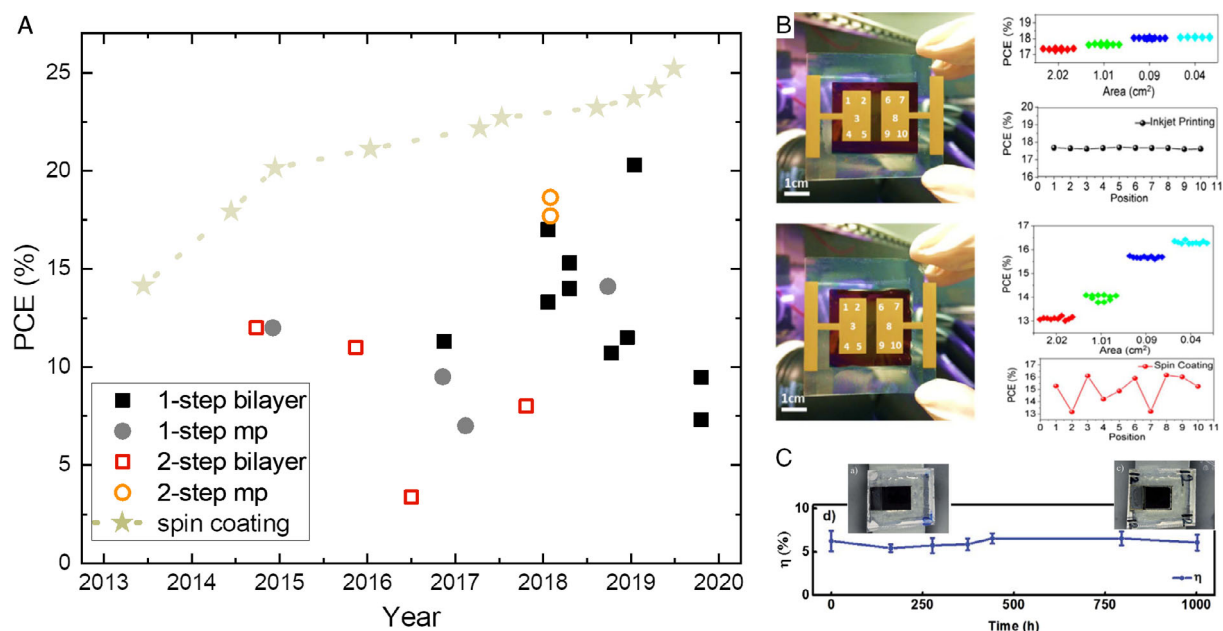


Figure 6. a) PCEs of lab-scale inkjet-printed PSCs. PCE values are extracted from J - V measurements. The publication with record efficiencies of different processes are marked. Other values are taken as following: 1-step bilayer devices from^[41,73,127,128,139,154–156]; 1-step on mesoporous/mesoscopic layers^[71,157–160]; 2-step bilayer^[92,100,128,146]; 2-step on mesoporous/mesoscopic layers^[126]. b) Comparison of inkjet-printed (top) and spin-coated (bottom) MAPbI₃ PSCs. Printed SCs show higher layer homogeneity and less PCE decrease with area increase.^[126] c) Long-term stability over 1000 h of inkjet-printed mesoscopic PSCs. Photographs at 0 h and after 1002 h. Reproduced with permission.^[158] Copyright 2017, Royal Society of Chemistry.

wetting and higher defect generation in the MAPbI₃ film. In addition, the devices with C₆₀ interlayer exhibit higher charge carrier extraction and reduced carrier recombination indicated by a lower series resistance. Increasing the device area from 0.04 to 4 cm² results in a decrease in PCE to 13.27% (–20%) for inkjet-printed devices, which is less compared with spin-coated devices with a reduction from –70 to 90%. The next step was to utilize cesium-containing triple cation perovskite to increase the PCE. Mathies et al. developed a tertiary ink, containing DMSO, DMF, and GBL to print a cesium-containing triple cation recipe, which was introduced by Saliba et al. With the vacuum solvent extraction method, PCEs of up to 15.3% are achieved.^[154] The main limitation was found to be that grains horizontally fragmented (exhibit grain boundaries) in the direction of the charge carrier transport direction, which decreased the FF below 70%. Nevertheless, a V_{OC} above 1.1 V could be observed in planar n-i-p architecture (TiO₂/perovskite/Spiro-MeOTAD). Building upon these results with slight adjustments of the ink recipe, Abzieher et al.^[156] achieved 20.7% PCE with a steady-state maximum power point of 18.5% in triple cation inkjet-printed perovskite layers on electron-beam deposited nickel oxide hole-transporting contacts. NiO_x offers good wettability, electrical transport properties, high stability, and the MHP layer exhibited pillar-like grains throughout the 1 μm film thickness. Devices also exhibit promising long-time performance with the PCE only being reduced by relative 12% after an exposure time of about 4100 sun hours (which corresponds to a lifetime of more than 2 years in Germany). Further progress was achieved by Huckaba et al. who used a perovskite absorber layer consisting

of four cations: Cs, Gu, MA, and FA.^[160] While guanidinium was shown to improve the stability of perovskite devices, Cs stabilizes the perovskite crystal structure and the film formation. The optimized ink formulation is further improved by adding small amounts of NMP and 0.1% m/m of the surfactant (phosphatidylcholine) to the DMF/DMSO/GBL solvent mixture. This solvent mixture was observed to provide good wetting on the inkjet-printed TiO₂ film surface and good control over the morphology and film thickness. Alternatively, to the vacuum treatment, the printed layers were crystallized by an antisolvent treatment, in this case, dipping the inkjet-printed sample in diethyl ether to generate the intermediate perovskite species and remove excess ink so that the film could then be annealed to yield a highly crystalline perovskite film. With increasing ink concentration, an increase in layer thickness, absorption, and J_{SC} is measured. An optimal concentration of 0.92 M is found to maximize the PCE to 12%. Higher concentrations result in drastic reduction of FF and V_{OC}, due to increasing parasitic absorption. Trudeau et al.^[159] presented inkjet-printed perovskite layers and hole transport layer (HTL) toward fully printed PSCs. An industrial large volume compatible inkjet printer (Ceradrop F-series) is used to print chloride containing perovskite ink on a mesoporous TiO₂ layer. In addition, Spiro-MeOTAD and the epoxy-based photoresist SU-8 as encapsulation layer is inkjet-printed on top. While the PCE of the first devices is below 0.1%, Trudeau et al. show a possible route for all inkjet-printed PSC. Gheno et al. reported the first (except of the electrodes) fully inkjet-printed PSC with WO₃/perovskite/Spiro-MeOTAD.^[41] To improve the wettability of the printed WO₃ layer and increase the

layer uniformity, diiodooctane is added to the MAI-containing perovskite ink. The efficiency of fully printed devices with a 1800 nm-thick perovskite layer shows a PCE of 10.7% but with large hysteresis (6.4% in forward direction), low V_{OC} of 0.75 V and comparable low light stability. This is mainly due to the detrimental influence of the photocatalytic properties of WO_3 . WO_3 devices are found to be more sensitive than TiO_2 to ambient moisture under illumination, leading to a rapid decrease in photocurrent during operation.^[41,83] The presence of water molecules is indeed revealed in the perovskite active layer through photoluminescence measurements. A future application of PSC is shown by Schlisske et al., where they stacked an inkjet-printed PSC with an inkjet-printed fluorescent dye layer together to show a possible application of fully printed colorful building integrated photovoltaics.^[155] The luminescent downshifting dye was printed on the rear side of the PSC, to shift absorbed light to lower energy, where it can be more efficiently converted to electrical power. In addition, the color perception of the brown/black PSC is tuned to various colors from red, green to blue.

4.1.3. Mesoscopic Solar Cells

Another approach to achieve fully printable PSCs is utilizing mesoscopic solar cells, shown by Hashmi et al. By infiltrating $MAPbI_3$ into a 2–10 μm -thick mesoporous scaffold of electron transport layer TiO_2 , an insulator ZrO_2 and carbon-based HTL/electrode, a PCE of 9.53% is achieved.^[157] The carbon-based perovskite solar cell (CPSC) is fully printed with spray-coated TiO_2 , screen-printed ZrO_2 , and inkjet-printed perovskite/carbon layer. The device shows a lack of J_{SC} with only 15 mA cm^{-2} and V_{OC} below 1 V, due to nonoptimized crystallization in the scaffold pores. Hashmi et al. further developed the concept with screen printing the mesoporous TiO_2 and ZrO_2 layer.^[158] The perovskite ink containing MAI, PbI_2 , and 5-AVAI is printed from GBL solution and is annealed for 1.5 h at 50°C under ambient conditions for full conversion to the black perovskite phase. The initial short-term stability (for the first 250 h) of this batch of CPSCs also suggested that despite the high porosity, the thick carbon (12–14 μm) and then thinner ZrO_2 (1–2 μm) were remarkably able to protect the perovskite light absorbing layer against the maintained humidity and ultraviolet (UV) illumination without any encapsulation. Furthermore, epoxy-sealed samples, including active and nonactive porous areas withstand 1002 h of 1.5 AM light soaking reaching a PCE of 8.6% (see Figure 6c). Meroni et al. are using a robotic mesh method (RbM), where they print a PbI_2 layer in a mesoscopic scaffold of mp- TiO_2 , mp- ZrO_2 , and carbon.^[147] The perovskite layer is formed after dipping the device into a MAI/IPA solution. To improve the film quality Meroni et al. print on top of a mesh, which is located on top of the mesoporous scaffold. The RbM method facilitates a uniform infiltration across the entire surface, and therefore, due to reduced pore clogging, an improved conversion to the $MAPbI_3$ phase during MAI immersion. The method was tested on the fully printable mesoscopic PSCs showing improved infiltration uniformity and control compared with the more common drop deposition, leading to a PCE as high as 9.8% on a 1 cm^2 device.

4.1.4. Lessons Learned

First successful demonstrations of using DoD IJP for the fabrication of PSCs have been achieved. The technology allows for direct patterning of printed layers from single micrometer drops to homogenous and compact layers. The depicted results indicate, that the IJP allows to print even complex multication systems by one-step or two-step method. A major benefit of IJP is the utilization of multihead systems to print different perovskite combinatorial compositions wet-in-wet. Therefore, a large number of halide or cation mixtures can be investigated by simply printing different ratios from inks loaded in different print-heads. Still, the main challenge is to induce a fast homogeneous nucleation, while delaying the crystal growth for thermodynamically favorable orientation and larger grains. Therefore, thorough preparation and functionalization of utilized substrates have to be considered, when using IJP. So far, the development of specific inks for use in IJP has not been the focus. In most cases, known solvent mixtures used for spin coating have been slightly modified to adapt them to the requirements of IJP. Nevertheless, the PCE of IJP solar cells caught up with record efficiencies reported by spin coating and overtook all other printing technologies.^[30] Over the past few years, most researches focused on one-step printing of triple cation perovskite ink with additional vacuum solvent extraction method, exhibiting highest PCE of 20.7%, which is only 4% behind best, spin-coated devices. Two-step processes only show high PCE when printing the underlying PbI_2 layer and inducing the crystallization by MAI vapor. Highly stable inkjet-printed devices with a PCE of 9% are processed in mesoscopic architecture showing more than 1000 h long-term stability against UV and moisture, comparable with devices utilizing similar perovskite precursors. Several approaches toward fully printed PSCs are shown, but without resounding success in terms of PCE. Major issue is the choice of orthogonal solvents to not dissolve the other layers. In addition, first examples of upscaling the inkjet-printed PSCs show its benefits with uniform layers and stable PCE up to 4 cm^2 . Larger devices or modules have not yet been reported in the literature. Nevertheless, IJP could be a part of futures PSC manufacturing as Saule Technologies installed first prototypes as building integrated PV in skyscrapers and indoor applications.^[161] In addition, the limited number of researchers, working in the field of IJP of PSCs, it seems that there is no intrinsic reason, why inkjet-printed PSCs could not reach the same PCE and stability level of spin-coated devices.

4.2. Lighting Applications

In addition to the vast usage of MHPs for photovoltaic applications, the optoelectronic properties of MHP are also interesting for lighting. The main advantage of IJP is the utilization of various perovskite structures within one processing technique. Smooth, uniform, and optical dense perovskite layers are also utilized in distributed feedback lasers, which Mathies et al. showed first in early 2018.^[162] They showed that it is possible to print $\approx 150 \text{ nm}$ thin perovskite layer with a layer roughness below 5 nm on a nanoimprinted grating on a flexible poly(ethylene terephthalate) (PET) substrate to build an optical pumped distributed

feedback laser. The measurable red laser emission of 784 nm and a bandwidth below 0.4 nm proves the excellent quality of inkjet-printed perovskite layer. Main advantage of the IJP technique is the possibility of printing large-area thin films, as well as micro-structured patterns. Gu et al. showed, that the crystal structure of CsPbBr₃ can be tuned by changing the concentration of the printed perovskite ink.^[117] At low temperatures (below 8 °C) on a low adhesive silicon surface, microplates of CsPbBr₃ are forming. Lasing with an emission wavelength of 548 to 553 nm with a threshold of 15.9 μJ cm⁻² is measured, when the microplate crystals (diameter 3.2–6.7 μm) are optically pumped by a 400 nm laser. On low adhesion-modified silicon surface, perovskite single crystal arrays in red–green–blue (RGB) color scheme are printed. Nanocrystals from CH₃NH₃PbBr₃ (green), a mixed-halide CH₃NH₃PbCl_xBr_{3-x} (blue), and CH₃NH₃PbBr_xI_{3-x} (red) are printed to visualize the RGB mode, when illuminated under UV light (402 nm) irradiation, as shown in **Figure 7a**. Full width at half maximums are located at 443 nm (blue), 532 nm (green), and 679 nm (red), respectively. Liu et al. synthesized CsPbBr₃ nanocrystals capped with polymeric polyvinylpyrrolidone (PVP) to have better control over the ink viscosity, size distribution, and crystallization.^[42] By controlling substrate temperature and the PVP amount, the outward capillary flow (coffering-effect) is

eliminated and CsPbBr₃ nanocrystals form metallic bonds with the C=O groups in PVP, leading to a uniform size distribution of PVP-capped nanoparticles in the precursor solution. The layer homogeneity of the nanocrystals is further optimized by an additional vacuum annealing step. The approach can be used for different halides and color perceptions, e.g., for anticounterfeiting applications. Sun et al. demonstrated an approach to realize confidential information protection based on the anion-exchange reaction of perovskite QDs.^[153] Luminescent CsPbX₃ QDs can be rapidly obtained from invisible halide salts, by simply reacting with a colorless developer, e.g., cubic CsPbCl₃ QDs. In addition, the conversion of luminescent 3D to colorless 0D perovskite allows to reversible quench (encryption) and restore (decryption) the luminescence of the patterns. Different halide seed layers have been printed and coated with cubic CsPbCl₃ QDs. In presence of iodide (bromide)-containing substrate, the CsPbCl₃ (peak emission at 479 nm) undergoes a halide exchange to CsPbI₃ (CsPbBr₃) and a peak luminesces at 640 nm (516 nm). The encryption by butylamine and decryption by acetic acid is described by a change in crystal structure from 3D (CsPbX₃) to 0D (Cs₄PbX₆) perovskite. After five cycles of decryption and encryption, 80% of initial PL is restored. **Figure 7b** shows the different colors and decryption and encryption processes. Wong et al. used a

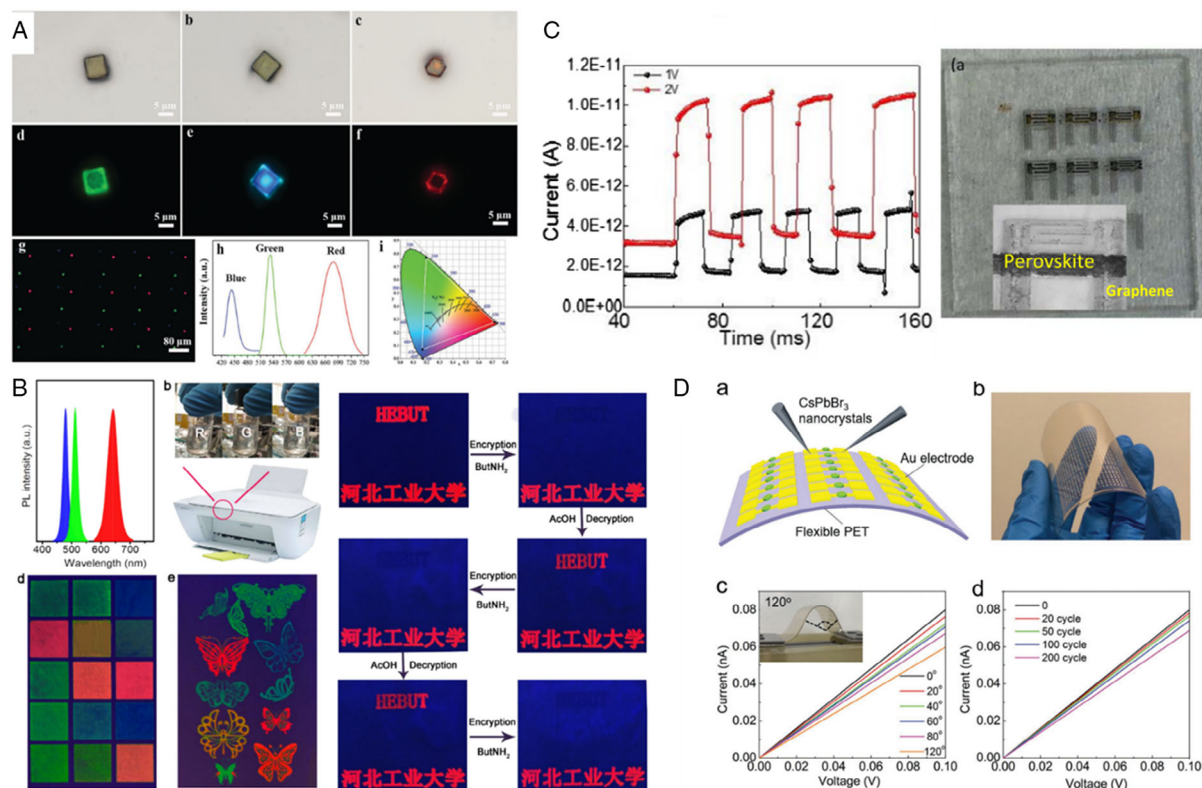


Figure 7. a) Bright field (top) and fluorescence (middle) microscope images and emission spectra and color gamut spectra (bottom) of RGB perovskite single crystals. Green: MAPbBr₃, blue: MAPbCl_{2.4}Br_{0.6}, and red: MAPbI_{0.43}Br_{2.57}. Reproduced with permission.^[117] Copyright 2017, Wiley-VCH. b) PL spectra and fluorescent photos of sophisticated patterns of red, green, and blue ink printed on paper. Encryption and decryption processes of the red letters "HEBUT." Adapted with permission.^[153] Copyright 2019, American Chemical Society. c) ON/OFF ratio and optical image of an inkjet-printed perovskite/graphene photodetector. Reproduced with permission.^[163] Copyright 2019, IEEE. d) Schematic and optical images of an inkjet-printed flexible soft X-ray detector utilizing CsPbBr₃ QDs (top). I–V curves of the flexible device arrays at different bending angles and bending cycles (bottom) under the X-ray illumination of 7.33 mGy_{air} s⁻¹ and 0.1 V bias voltage. Reproduced with permission.^[164] Copyright 2019, Wiley-VCH.

light-mediated halide exchange for luminescent halide perovskites.^[152] Therefore, low concentrated greenish CsPbBr₃ nanocrystals were printed first. To tune the luminescent, organic halide sources, such as *tert*-butyl chloride or *tert*-butyl iodide, were diluted with cyclohexane, followed by the addition of thiophenol for PL enhancement and polystyrene to tune the viscosity of the solution. During the IJP of the organic halide source, the film was exposed to blue light (464 nm) to perform a photoactivated halide exchange reaction.

4.3. Sensor Applications

Alamri et al. reported on fully inkjet-printed photodetectors using a heterojunction of graphene/perovskite/graphene.^[163] The photodetector exhibited a high response of $R = 0.53 \text{ AW}^{-1}$ over the whole visible range, corresponding to a detectivity of $D = 3.4 \times 10^{10}$ Jones. The perovskite layer is formed at 90 °C from a DMF-based ink, containing chlorine spectator ions. The perovskite absorber layer is embedded in graphene crystal flakes with the perovskite basal surface parallel to the crystal facets. Figure 7c shows the ON/OFF ratio and an optical image of the printed photodetector. Liu et al. built a photodetector utilizing highly oriented and conductive perovskite microwires, by printing a CH₃NH₃PbI₃ in DMF/GBL precursor solution.^[70] These lateral photodetectors show a responsivity of 1.2 A W^{-1} , high detectivity of 2.39×10^{12} Jones, when illuminated at a light power density of 0.1 mW cm^{-2} and biased at 10 V. When the illumination intensity was increased to 7 mW cm^{-2} , photocurrent could be more than 1 μA, producing a photocurrent ON/OFF ratio of ≈ 1000 . Liu et al. utilized CsPbBr₃ perovskite QDs on SiO₂/Si substrates for soft X-ray detectors.^[164] CsPbBr₃ QDs were printed with a thickness of only 20 nm and surface roughness of around 4 nm in an Au/CsPbBr₃/Au structure on a silicon wafer. High sensitivities of up to $1450 \mu\text{C Gy}_{\text{air}}^{-1} \text{ cm}^{-2}$ are achieved under an X-ray dose rate of $17.2 \mu\text{Gy}_{\text{air}} \text{ s}^{-1}$ with only 0.1 V bias voltage. Further, Liu et al. presented a flexible X-ray detector on PET substrate. During bending, only a small loss in current was observed, mainly to stress of the material (see Figure 7d). The bending cycle test shows only a current degradation of 12% after 200 cycles, indicating the excellent conductivity, stability, and durability of the uniformly grown inkjet-printed perovskite film.

5. Conclusion

In conclusion, IJP allows for selectively depositing MHP in wide range of 2D and 3D structures forming a wide range of different crystal structures with defined electronic properties required for a range of electronic and optoelectronic applications. This ranges from printing nanocrystals from printed single droplets for light-emitting devices to large-area uniform and pinhole-free layers, utilized for photovoltaic devices. All these results demonstrate, that all the impressive optoelectronic properties of MHP found so far are also accessible via IJP processes. Nucleation and crystal growth of the MHPs are key elements in fabrication of MHP structures. Especially the coordination of solvents and precursor content have to be understood in more detail to effectively predict new strategies

for ink development, such as utilizing nontoxic solvents. In the area of photovoltaics, IJP is considered a feasible technology to also achieve high efficiency. In recent years, different strategies have been obtained, constantly improving the PCE and paving the way for highly efficient large-area solar modules. Sequential deposition of lead and halide compound combining printing and nonprinting techniques allowing for better control over crystallization and film formation. Nevertheless, most of the researches focused on one-step IJP processing, leading to record PCE exceeding 20%. Herein, all precursors are printed from one solution in combination with a fast and controlled removal of solvents by vacuum annealing seems to be the most efficient to achieve high-quality MHP thin films for photovoltaic devices. Thereby the development of slow drying inks that allows a delayed processing time to separate printing and drying of the MHP layers appears to be a necessary route. Nonetheless, IJP technology has to prove its high-level scalability to module sizes beyond 10 or better 100 cm² with decent efficiency values. In addition, IJP offers the possibility of depositing small and defined structures for other applications. Especially, for lighting, detector and sensing applications, microcrystals with tunable properties are desirable. IJP allows printing single crystals from volume-dependent drops, paving a route for commercialization of highly efficient perovskite X-ray and photodetector applications beyond the usage in PSCs.

Acknowledgements

The authors acknowledge the funding by the German Federal Ministry of Education and Research (BMBF), the Helmholtz Energy Materials Foundry (HEMF) and PEROSEED (ZT-0024) project as well as the support of the Helmholtz Innovation Lab HySPRINT. This work was conducted in the framework of the Joint Laboratory GEN_FAB. E.U. and F.M. acknowledge the funding from the German Ministry of Education and Research (BMBF) for the Young Investigator Group Hybrid Materials Formation and Scaling (HyPerFORME) within the program "NanoMatFutur" (Grant No. 03XP0091).

Conflict of Interest

The authors declare no conflict of interest.

Keywords

additive manufacturing, inkjet printing, light-emitting devices, optoelectronics, perovskites, solar cells

Received: August 19, 2019

Revised: October 25, 2019

Published online: December 3, 2019

- [1] F. Savart, *Ann. Chim.* **1833**, 53, 337.
- [2] C. W. Hansell, (Delaware), US2512743 **1946**.
- [3] G. Cummins, M. P. Y. Desmulliez, *Circuit World* **2012**, 38, 193.
- [4] F. Hermerschmidt, S. A. Choulis, E. J. W. List-Kratochvil, *Adv. Mater. Technol.* **2019**, 4, 1800474.
- [5] S. Gamerith, A. Klug, H. Scheiber, U. Scherf, E. Moderegger, E. J. W. List, *Adv. Funct. Mater.* **2007**, 17, 3111.

- [6] H. Sirringhaus, T. Kawase, R. H. Friend, T. Shimoda, M. Inbasekaran, W. Wu, E. P. Woo, *Science* **2000**, 290, 2123.
- [7] S. R. Forrest, *Nature* **2004**, 428, 911.
- [8] E. Tekin, P. J. Smith, U. S. Schubert, *Soft Matter* **2008**, 4, 703.
- [9] M. Touri, F. Kabirian, M. Saadati, S. Ramakrishna, M. Mozafari, *Adv. Eng. Mater.* **2019**, 21, 1800511.
- [10] E. Böhm, P. Levermore, H. Tseng, G. Bealle, H. Wang, P. Higon, H. Heil, A. Jatsch, H. Buchholz, M. Kгаа, F. Strasse, *SID Symp. Dig. Tech. Pap.* **2017**, 842.
- [11] Kateeva, Kateeva webpage, <http://kateeva.com/> (accessed: October 2019).
- [12] J. Hebb, *Advanced Inkjet Printing: Enabling The OLED Revolution*, Kateeva Inc., San Jose **2017**.
- [13] R. Mertens, Inkjet printed OLED mass production process in 2020, <https://www.oled-info.com/ihs-ink-jet-printing-finally-become-mass-production-oled-production-process-2020> (accessed: October 2019).
- [14] S. K. Karunakaran, G. M. Arumugam, W. Yang, S. Ge, S. N. Khan, X. Lin, G. Yang, *J. Mater. Chem. A* **2019**, 13873–13902.
- [15] M. Singh, H. M. Haverinen, P. Dhagat, G. E. Jabbour, *Adv. Mater.* **2010**, 22, 673.
- [16] S. Sumaiya, K. Kardel, A. El-Shahat, *Technologies* **2017**, 5, 53.
- [17] X. Lin, J. Kavalakkatt, M. C. Lux-Steiner, A. Ennaoui, *Adv. Sci.* **2015**, 2, 2.
- [18] M. Colina, E. Bailo, B. Medina-Rodríguez, R. Kondrotas, Y. Sánchez-González, D. Sylla, M. Placidi, M. Blanes, F. Ramos, A. Cirera, A. Pérez Rodríguez, E. Saucedo, *J. Alloys Compd.* **2018**, 735, 2462.
- [19] X. Lin, V. E. Madhavan, J. Kavalakkatt, V. Hinrichs, I. Lauer mann, M. C. Lux-Steiner, A. Ennaoui, R. Klenk, *Sol. Energy Mater. Sol. Cells* **2018**, 180, 373.
- [20] T. Martini, C. Chubilleau, O. Poncelet, A. Ricaud, A. Blayo, C. Martin, K. Tarasov, *Sol. Energy Mater. Sol. Cells* **2016**, 144, 657.
- [21] T. K. Chaudhuri, M. H. Patel, D. Tiwari, P. R. Ghediya, *J. Alloys Compd.* **2018**, 747, 31.
- [22] X. Lin, J. Kavalakkatt, N. Brusten, M. C. Lux-steiner, A. Ennaoui, *29th Eur. Photovolt. Sol. Energy Conf. Exhib.* **2014**, 1, 1876.
- [23] J. Barbé, J. Eid, E. Ahlswede, S. Spiering, M. Powalla, R. Agrawal, S. Del Gobbo, *J. Nanopart. Res.* **2016**, 18, 379.
- [24] B. S. Yadav, S. Ranjan Day, S. R. Dhage, *Mater. Today Proc.* **2017**, 4, 12480.
- [25] W. Wang, Y. W. Su, C. H. Chang, *Sol. Energy Mater. Sol. Cells* **2011**, 95, 2616.
- [26] Y. Wang, X. Lin, L. Wang, T. Köhler, M. C. Lux-Steiner, R. Klenk, *Phys. Status Solidi Curr. Top. Solid State Phys.* **2017**, 14, 9.
- [27] NREL, NREL efficiency chart, <http://www.nrel.gov/ncpv/images/efficiency-chart.jpg> (accessed: October 2019).
- [28] E. L. Unger, O. Shargaieva, S. Braunger, P. Docampo, *Solar Energy Capture Materials*, The Royal Society of Chemistry, London **2019**, pp. 153–192.
- [29] Y. S. Jung, K. Hwang, Y. J. Heo, J. E. Kim, D. Vak, D. Y. Kim, *Adv. Opt. Mater.* **2018**, 1701182, 1.
- [30] I. A. Howard, T. Abzieher, I. M. Hossain, H. Eggers, F. Schackmar, S. Ternes, B. S. Richards, U. Lemmer, U. W. Paetzold, *Adv. Mater.* **2019**, 31, 1806702.
- [31] R. Swartwout, M. T. Hoerantner, V. Bulovi, *Energy Environ. Mater.* **2019**, 2, 119.
- [32] A. Klug, P. Patter, K. Popovic, A. Blümel, S. Sax, M. Lenz, O. Glushko, M. J. Cordill, E. J. W. List-Kratochvil, *Printed Memory and Circuits*, International Society for Optics and Photonics, Bellingham, WA **2015**, p. 95690N.
- [33] G. H. McKinley, M. Renardy, *Phys. Fluids* **2011**, 23, 127101.
- [34] B. Derby, *Annu. Rev. Mater. Res.* **2010**, 40, 395.
- [35] N. Reis, C. Ainsley, B. Derby, *J. Appl. Phys.* **2005**, 97, 094903.
- [36] K. S. Kwon, W. Kim, *Sens. Actuators A Phys.* **2007**, 140, 75.
- [37] D. Jang, D. Kim, J. Moon, *Langmuir* **2009**, 25, 2629.
- [38] D. K. Owens, R. C. Wendt, *J. Appl. Polym. Sci.* **1969**, 13, 1741.
- [39] W. Rabel, *Farbe und Lack* **1971**, 77, 997.
- [40] D. H. Kaelble, *J. Adhes.* **1970**, 2, 66.
- [41] A. Gheno, Y. Huang, J. Bouclé, B. Ratier, A. Rolland, J. Even, S. Vedraïne, *Sol. RRL* **2018**, 2, 1800191.
- [42] Y. Liu, F. Li, L. Qiu, K. Yang, Q. Li, X. Zheng, H. Hu, T. Guo, C. Wu, T. W. Kim, *ACS Nano* **2019**, 13, 2042.
- [43] Y. Sun, *Chem. Soc. Rev.* **2013**, 42, 2497.
- [44] W. A. Dunlap-Shohl, Y. Zhou, N. P. Padture, D. B. Mitzi, *Chem. Rev.* **2018**, 119, 3193.
- [45] V. K. LaMer, R. H. Dinegar, *J. Am. Chem. Soc.* **1950**, 72, 4847.
- [46] M. Jung, S.-G. Ji, G. Kim, S. Il Seok, *Chem. Soc. Rev.* **2019**, 48, 2011.
- [47] Y. Zhou, O. S. Game, S. Pang, N. P. Padture, *J. Phys. Chem. Lett.* **2015**, 6, 4827.
- [48] S. Ahmad, P. K. Kanaujia, W. Niu, J. J. Baumberg, G. Vijaya Prakash, *ACS Appl. Mater. Interfaces* **2014**, 6, 10238.
- [49] B. Charles, J. Dillon, O. J. Weber, M. S. Islam, M. T. Weller, *J. Mater. Chem. A* **2017**, 5, 22495.
- [50] H. Ko, D. H. Sin, M. Kim, K. Cho, *Chem. Mater.* **2017**, 29, 1165.
- [51] K. H. Stone, A. Gold-parker, V. L. Pool, E. L. Unger, A. R. Bowring, M. D. McGehee, M. F. Toney, C. J. Tassone, *Nat. Commun.* **2018**, 9, 3458.
- [52] M. Avrami, *J. Chem. Phys.* **1939**, 7, 1103.
- [53] M. Avrami, *J. Chem. Phys.* **1940**, 8, 212.
- [54] M. Avrami, *J. Chem. Phys.* **1941**, 9, 177.
- [55] S. Rahimnejad, A. Kovalenko, S. M. Forés, C. Aranda, A. Guerrero, *ChemPhysChem* **2016**, 17, 2795.
- [56] K. G. Stamplecoskie, J. S. Manser, P. V. Kamat, *Energy Environ. Sci.* **2015**, 8, 208.
- [57] S. J. Yoon, K. G. Stamplecoskie, P. V. Kamat, *J. Phys. Chem. Lett.* **2016**, 7, 1368.
- [58] J. H. Heo, M. H. Lee, M. H. Jang, S. H. Im, *J. Mater. Chem. A* **2016**, 4, 17636.
- [59] M. Yang, Z. Li, M. O. Reese, O. G. Reid, D. H. Kim, S. Siol, T. R. Klein, Y. Yan, J. J. Berry, M. F. A. M. Van Hest, K. Zhu, *Nat. Energy* **2017**, 2, 17038.
- [60] J. Lee, H. Kim, N. Park, *Acc. Chem. Res.* **2016**, 49, 311.
- [61] N. Ahn, D. Y. Son, I. H. Jang, S. M. Kang, M. Choi, N. G. Park, *J. Am. Chem. Soc.* **2015**, 137, 8696.
- [62] H.-B. Kim, H. Choi, J. Jeong, S. Kim, B. Walker, S. Song, J. Y. Kim, *Nanoscale* **2014**, 6, 6679.
- [63] D. Shen, X. Yu, X. Cai, M. Peng, Y. Ma, X. Su, L. Xiao, D. Zou, *J. Mater. Chem. A* **2014**, 2, 20454.
- [64] K. L. Gardner, J. G. Tait, T. Merckx, W. Qiu, U. W. Paetzold, L. Kootstra, M. Jaysankar, R. Gehlhaar, D. Cheyens, P. Heremans, J. Poortmans, *Adv. Energy Mater.* **2016**, 6, 1600386.
- [65] A. Babaei, L. Alberio-Blanquer, A. M. Igual-Muñoz, D. Pérez-Del-Rey, M. Sessolo, H. J. Bolink, R. Tadmouri, *Polyhedron* **2018**, 147, 9.
- [66] J. C. Hamill, J. Schwartz, Y. L. Loo, *ACS Energy Lett.* **2018**, 3, 92.
- [67] S. E. Denmark, G. L. Beutner, *ChemInform*, **39**, **2008**.
- [68] N. J. Jeon, J. H. Noh, Y. C. Kim, W. S. Yang, S. Ryu, S. Il Seok, *Nat. Mater.* **2014**, 13, 897.
- [69] Y. Jo, K. S. Oh, M. Kim, K. Kim, H. Lee, C. Lee, D. S. Kim, *Adv. Mater. Interfaces* **2016**, 3, 1500768.
- [70] Y. Liu, F. Li, C. P. Veeramalai, W. Chen, T. Guo, C. Wu, T. W. Kim, *ACS Appl. Mater. Interfaces* **2017**, 9, 11662.
- [71] S.-G. Li, K.-J. Jiang, M.-J. Su, X.-P. Cui, J.-H. Huang, Q.-Q. Zhang, X.-Q. Zhou, L.-M. Yang, Y.-L. Song, *J. Mater. Chem. A* **2015**, 3, 9092.
- [72] E. L. Unger, A. R. Bowring, C. J. Tassone, V. L. Pool, A. Gold-parker, R. Cheacharoen, K. H. Stone, E. T. Hoke, M. F. Toney, M. D. McGehee, *Chem. Mater.* **2014**, 26, 7158.

- [73] S. Chen, L. Zhang, L. Yan, X. Xiang, X. Zhao, S. Yang, B. Xu, *Adv. Funct. Mater.* **2019**, 1905487, 1905487.
- [74] M. Spina, E. Bonvin, A. Sienkiewicz, L. Forró, E. Horváth, *Sci. Rep.* **2016**, 6, 19834.
- [75] E. Horváth, M. Spina, Z. Szekrényes, K. Kamarás, R. Gaal, D. Gachet, L. Forró, *Nano Lett.* **2014**, 14, 6761.
- [76] I. Burgués-Ceballos, A. Savva, E. Georgiou, K. Kapnisis, P. Papagiorgis, A. Mousikou, G. Itskos, A. Othonos, S. A. Choulis, I. Burgú Es-Ceballos, *Appl. Phys. Lett. AIP Adv.* **2017**, 7, 115304.
- [77] J. Wang, F. Di Giacomo, J. Brüls, H. Gorter, I. Katsouras, P. Groen, R. A. J. Janssen, R. Andriessen, Y. Galagan, *Sol. RRL* **2017**, 1, 1700091.
- [78] T. J. Jacobsson, J. P. Correa-Baena, E. Halvani Anaraki, B. Philippe, S. D. Stranks, M. E. F. Bouduban, W. Tress, K. Schenk, J. Teuscher, J. E. Moser, H. Rensmo, A. Hagfeldt, *J. Am. Chem. Soc.* **2016**, 138, 10331.
- [79] G. Yang, H. Zhang, G. Li, G. Fang, *Nano Energy* **2019**, 63, 103835.
- [80] J. S. Manser, M. I. Saidaminov, J. A. Christians, O. M. Bakr, P. V. Kamat, *Acc. Chem. Res.* **2016**, 49, 330.
- [81] R. J. Stewart, C. Grieco, A. V. Larsen, G. S. Doucette, J. B. Asbury, *J. Phys. Chem. C* **2016**, 120, 12392.
- [82] J. M. Ball, M. M. Lee, A. Hey, H. J. Snaith, *Energy Environ. Sci.* **2013**, 6, 1739.
- [83] A. Gheno, T. Thi, T. Pham, C. Di Bin, J. Bouclé, B. Ratier, S. Vedraïne, *Sol. Energy Mater. Sol. Cells* **2017**, 161, 347.
- [84] M. Saliba, T. Matsui, J.-Y. Seo, K. Domanski, J.-P. Correa-Baena, M. K. Nazeeruddin, S. M. Zakeeruddin, W. Tress, A. Abate, A. Hagfeldt, M. Grätzel, *Energy Environ. Sci.* **2016**, 9, 1989.
- [85] M. Deepa, M. Salado, L. Calio, S. Kazim, S. M. Shivaprasad, S. Ahmad, *Phys. Chem. Chem. Phys.* **2017**, 19, 4069.
- [86] C. Yi, J. Luo, S. Meloni, A. Boziki, N. Ashari-Astani, C. Grätzel, S. M. Zakeeruddin, U. Röthlisberger, M. Grätzel, *Energy Environ. Sci.* **2016**, 9, 656.
- [87] J. W. Lee, D. H. Kim, H. S. Kim, S. W. Seo, S. M. Cho, N. G. Park, *Adv. Energy Mater.* **2015**, 5, 1501310.
- [88] T. Duong, Y. Wu, H. Shen, J. Peng, X. Fu, D. Jacobs, E. Wang, T. C. Kho, K. C. Fong, M. Stocks, E. Franklin, A. Blakers, N. Zin, K. McIntosh, W. Li, Y. Cheng, T. P. White, K. Weber, K. Catchpole, *Adv. Energy Mater.* **2017**, 1700228, 1700228.
- [89] M. Saliba, T. Matsui, K. Domanski, J.-Y. Seo, A. Ummadisingu, S. M. Zakeeruddin, J.-P. Correa-Baena, W. R. Tress, A. Abate, A. Hagfeldt, M. Grätzel, *Science* **2016**, 354, 206.
- [90] M. Zhang, J. S. Yun, Q. Ma, J. Zheng, C. F. J. Lau, X. Deng, J. Kim, D. Kim, J. Seidel, M. A. Green, S. Huang, A. W. Y. Ho-Baillie, *ACS Energy Lett.* **2017**, 2, 438.
- [91] S. Gholipour, A. M. Ali, J. P. Correa-Baena, S. H. Turren-Cruz, F. Tajabadi, W. Tress, N. Taghavinia, M. Grätzel, A. Abate, F. De Angelis, C. A. Gaggioli, E. Mosconi, A. Hagfeldt, M. Saliba, *Adv. Mater.* **2017**, 29, 1702005.
- [92] M. Bag, Z. Jiang, L. A. Renna, S. P. Jeong, V. M. Rotello, D. Venkataraman, *Mater. Lett.* **2016**, 164, 472.
- [93] N. J. Jeon, J. H. Noh, W. S. Yang, Y. C. Kim, S. Ryu, J. Seo, S. Il Seok, *Nature* **2015**, 517, 476.
- [94] L. Zhao, N. Rolston, K. M. Lee, X. Zhao, M. A. Reyes-Martinez, N. L. Tran, Y. W. Yeh, N. Yao, G. D. Scholes, Y. L. Loo, A. Selloni, R. H. Dauskardt, B. P. Rand, *Adv. Funct. Mater.* **2018**, 28, 1.
- [95] X. Hou, Y. Hu, H. Liu, A. Mei, X. Li, M. Duan, G. Zhang, Y. Rong, H. Han, *J. Mater. Chem. A* **2017**, 5, 73.
- [96] N. Giesbrecht, J. Schlipf, I. Grill, P. Rieder, V. Dyakonov, T. Bein, A. Hartschuh, P. Müller-Buschbaum, P. Docampo, *J. Mater. Chem. A* **2018**, 6, 4822.
- [97] W. Zhang, M. Saliba, D. T. Moore, S. K. Pathak, M. T. Hörantner, T. Stergiopoulos, S. D. Stranks, G. E. Eperon, J. A. Alexander-Webber, A. Abate, A. Sadhanala, S. Yao, Y. Chen, R. H. Friend, L. A. Estroff, U. Wiesner, H. J. Snaith, *Nat. Commun.* **2015**, 6, 1.
- [98] J. G. Tait, S. Manghooli, W. Qiu, L. Rakocevic, L. Kootstra, M. Jaysankar, C. A. Masse de la Huerta, U. W. Paetzold, R. Gehlhaar, D. Cheyng, P. Heremans, J. Poortmans, *J. Mater. Chem. A* **2016**, 4, 3792.
- [99] E. Parvazian, A. Abdollah-zadeh, M. Dehghani, N. Taghavinia, *ACS Appl. Energy Mater.* **2019**, 9, 6209.
- [100] T. Abzieher, F. Mathies, M. Hetterich, A. Welle, D. Gerthsen, U. Lemmer, U. W. Paetzold, M. Powalla, *Phys. Status Solidi Appl. Mater. Sci.* **2017**, 214, 1700509.
- [101] Z. Xiao, D. Wang, Q. Dong, Q. Wang, W. Wei, J. Dai, X. Zeng, J. Huang, *Energy Environ. Sci.* **2016**, 9, 867.
- [102] I. Levchuk, Y. Hou, M. Gruber, M. Brandl, P. Herre, X. Tang, F. Hoegl, M. Batentschuk, A. Osvet, R. Hock, W. Peukert, R. R. Tykwinski, C. J. Brabec, *Adv. Mater. Interfaces* **2016**, 3, 1.
- [103] W. Zhang, S. Pathak, N. Sakai, T. Stergiopoulos, P. K. Nayak, N. K. Noel, A. A. Haghighirad, V. M. Burlakov, D. W. deQuilettes, A. Sadhanala, W. Li, L. Wang, D. S. Ginger, R. H. Friend, H. J. Snaith, *Nat. Commun.* **2015**, 6, 10030.
- [104] Y. Hu, S. Si, A. Mei, Y. Rong, H. Liu, X. Li, H. Han, *Sol. RRL* **2017**, 1, 160019.
- [105] J. H. Heo, D. H. Song, S. H. Im, *Adv. Mater.* **2014**, 26, 8179.
- [106] D. P. McMeekin, Z. Wang, W. Rehman, F. Pulvirenti, J. B. Patel, N. K. Noel, M. B. Johnston, S. R. Marder, L. M. Herz, H. J. Snaith, *Adv. Mater.* **2017**, 29, 1607039.
- [107] J. Pan, C. Mu, Q. Li, W. Li, D. Ma, D. Xu, *Adv. Mater.* **2016**, 28, 8309.
- [108] G. E. Eperon, S. D. Stranks, C. Menelaou, M. B. Johnston, L. M. Herz, H. J. Snaith, *Energy Environ. Sci.* **2014**, 7, 982.
- [109] C. Zuo, L. Ding, *Nanoscale* **2014**, 6, 9935.
- [110] Y. Chen, Y. Zhao, Z. Liang, *Chem. Mater.* **2015**, 27, 1448.
- [111] J. Dagar, K. Hirslandt, A. Merdasa, A. Czudek, R. Munir, F. Zu, N. Koch, T. Dittrich, E. L. Unger, *Sol. RRL* **2019**, 1900088.
- [112] K. M. Boopathi, M. Ramesh, T.-Y. Huang, W. Budiawan, M. Y. Lin, C.-H. Lee, K.-C. Ho, C. W. Chu, *J. Mater. Chem. A* **2016**, 4, 1591.
- [113] C.-C. Chueh, C.-Y. Liao, F. Zuo, S. T. Williams, P.-W. Lianga, A. K.-Y. Jen, *J. Mater. Chem. A* **2015**, 3, 9058.
- [114] P.-W. Liang, C.-Y. Liao, C.-C. Chueh, F. Zuo, S. T. Williams, X.-K. Xin, J. Lin, A. K.-Y. Jen, *Adv. Mater.* **2014**, 26, 3748.
- [115] A. Giuri, E. Saleh, A. Listorti, S. Colella, A. Rizzo, C. Tuck, C. E. Corcione, *Nanomaterials* **2019**, 9, 582.
- [116] A. Giuri, S. Masi, A. Listorti, G. Gigli, S. Colella, C. Esposito Corcione, A. Rizzo, *Nano Energy* **2018**, 54, 400.
- [117] Z. Gu, K. Wang, H. Li, M. Gao, L. Li, M. Kuang, Y. S. Zhao, M. Li, Y. Song, *Small* **2017**, 13, 1603217.
- [118] A. Chandramohan, S. Dash, J. A. Weibel, X. Chen, S. V. Garimella, *Langmuir* **2016**, 32, 4729.
- [119] Y. Li, Q. Yang, M. Li, Y. Song, *Sci. Rep.* **2016**, 6, 1.
- [120] Y. Tidhar, E. Edri, H. Weissman, D. Zohar, G. Hodes, D. Cahen, B. Rybtchinski, S. Kirmayer, *J. Am. Chem. Soc.* **2014**, 136, 13249.
- [121] M. E. R. Shanahan, *Langmuir* **1995**, 11, 1041.
- [122] S. Feng, S. Wang, L. Gao, G. Li, Y. Hou, Y. Zheng, *Angew. Chem. Int. Ed.* **2014**, 53, 6163.
- [123] C. Bi, Q. Wang, Y. Shao, Y. Yuan, Z. Xiao, J. Huang, *Nat. Commun.* **2015**, 6, 1.
- [124] S. Zhang, M. Stolterfoht, A. Armin, Q. Lin, F. Zu, J. Sobus, H. Jin, N. Koch, P. Meredith, P. L. Burn, D. Neher, *ACS Appl. Mater. Interfaces* **2018**, 10, 21681.

- [125] M. Schultes, N. Giesbrecht, J. Küffner, E. Ahlswede, P. Docampo, T. Bein, M. Powalla, *ACS Appl. Mater. Interfaces* **2019**, *11*, 12948.
- [126] P. Li, C. Liang, B. Bao, Y. Li, X. Hu, Y. Wang, Y. Zhang, F. Li, G. Shao, Y. Song, *Nano Energy* **2018**, *46*, 203.
- [127] F. Mathies, T. Abzieher, A. Hochstuhl, K. Glaser, A. Colsmann, U. W. Paetzold, G. Hernandez-Sosa, U. Lemmer, A. Quintilla, *J. Mater. Chem. A* **2016**, *4*, 19207.
- [128] Z. Jiang, M. Bag, L. Renna, S. P. Jeong, D. Venkataraman, Z. Jiang, M. Bag, L. Renna, S. P. Jeong, V. Rotello, HAL **2016**, hal-01386295.
- [129] M. Saliba, T. Matsui, J.-Y. Seo, K. Domanski, J.-P. Correa-Baena, M. K. Nazeeruddin, S. M. Zakeeruddin, W. Tress, A. Abate, A. Hagfeldt, M. Grätzel, *Energy Environ. Sci.* **2016**, *9*, 1989.
- [130] M. Saliba, J. P. Correa-Baena, C. M. Wolff, M. Stollerfoht, N. Phung, S. Albrecht, D. Neher, A. Abate, *Chem. Mater.* **2018**, *30*, 4193.
- [131] Y. Deng, Q. Wang, Y. Yuan, J. Huang, *Mater. Horiz.* **2015**, *2*, 578.
- [132] N. K. Noel, S. N. Habisreutinger, B. Wenger, M. T. Klug, M. T. Hö, M. B. Johnston, R. J. Nicholas, D. T. Moore, H. J. Snaith, *Energy Environ. Sci.* **2017**, *10*, 1.
- [133] A. Babayigit, J. D'Haen, H. G. Boyen, B. Conings, *Joule* **2018**, *2*, 1205.
- [134] B. Conings, A. Babayigit, M. T. Klug, S. Bai, N. Gauquelin, N. Sakai, J. T.-W. Wang, J. Verbeeck, H.-G. Boyen, H. J. Snaith, *Adv. Mater.* **2016**, *28*, 10701.
- [135] F. Huang, Y. Dkhissi, W. Huang, M. Xiao, I. Benesperi, S. Rubanov, Y. Zhu, X. Lin, L. Jiang, Y. Zhou, A. Gray-Weale, J. Etheridge, C. R. McNeill, R. A. Caruso, U. Bach, L. Spiccia, Y.-B. Cheng, *Nano Energy* **2014**, *10*, 10.
- [136] T. Zhang, N. Guo, G. Li, X. Qian, L. Li, Y. Zhao, *J. Mater. Chem. A* **2016**, *4*, 3245.
- [137] F. Zhang, J. Song, L. Zhang, F. Niu, Y. Hao, P. Zeng, H. Niu, J. Huang, J. Lian, *J. Mater. Chem. A* **2016**, *4*, 8554.
- [138] X. Li, D. Bi, C. Yi, J.-D. Decoppet, J. Luo, S. M. Zakeeruddin, A. Hagfeldt, M. Grätzel, *Science* **2016**, *353*, 58.
- [139] C. Liang, P. Li, H. Gu, Y. Zhang, F. Li, Y. Song, G. Shao, N. Mathews, G. Xing, *Sol. RRL* **2018**, *2*, 1770150.
- [140] J. H. Im, H. S. Kim, N. G. Park, *APL Mater.* **2014**, *2*, 081510.
- [141] K. Liang, D. B. Mitzi, M. T. Prikas, *Chem. Mater.* **1998**, *10*, 403.
- [142] J.-H. Im, I.-H. Jang, N. Pellet, M. Grätzel, N.-G. Park, *Nat. Nanotechnol.* **2014**, *9*, 927.
- [143] J. Schlipf, P. Docampo, C. J. Schaffer, V. Körstgens, L. Bießmann, F. Hanusch, N. Giesbrecht, S. Bernstorff, T. Bein, P. Müller-Buschbaum, *J. Phys. Chem. Lett.* **2015**, *6*, 1265.
- [144] L. Oesinghaus, J. Schlipf, N. Giesbrecht, L. Song, Y. Hu, T. Bein, P. Docampo, P. Müller-Buschbaum, *Adv. Mater. Interfaces* **2016**, *3*, 1600403.
- [145] S. Yang, Y. C. Zheng, Y. Hou, X. Chen, Y. Chen, Y. Wang, H. Zhao, H. G. Yang, *Chem. Mater.* **2014**, *26*, 6705.
- [146] Z. Wei, H. Chen, K. Yan, S. Yang, *Angew. Chem. Int. Ed.* **2014**, *53*, 13239.
- [147] S. M. P. Meroni, Y. Mouhamad, F. De Rossi, A. Pockett, J. Baker, R. Escalante, J. Searle, M. J. Carnie, E. Jewell, G. Oskam, T. M. Watson, *Sci. Technol. Adv. Mater.* **2018**, *19*, 1.
- [148] Y. Wu, A. Islam, X. Yang, C. Qin, J. Liu, K. Zhang, W. Peng, L. Han, *Energy Environ. Sci.* **2014**, *7*, 2934.
- [149] W. Fu, J. Yan, Z. Zhang, T. Ye, Y. Liu, J. Wu, J. Yao, C. Z. Li, H. Li, H. Chen, *Sol. Energy Mater. Sol. Cells* **2016**, *155*, 331.
- [150] J. Cao, X. Jing, J. Yan, C. Hu, R. Chen, J. Yin, J. Li, N. Zheng, *J. Am. Chem. Soc.* **2016**, *138*, 9919.
- [151] H. S. Ko, J. W. Lee, N. G. Park, *J. Mater. Chem. A* **2015**, *3*, 8808.
- [152] Y. Wong, W. Wu, T. Wang, J. D. A. Ng, K. H. Khoo, J. Wu, Z. Tan, *Adv. Mater.* **2019**, 1901247, 1901247.
- [153] C. Sun, S. Su, Z. Gao, H. Liu, H. Wu, X. Shen, W. Bi, *ACS Appl. Mater. Interfaces* **2019**, *11*, 8210.
- [154] F. Mathies, H. Eggers, B. S. Richards, G. Hernandez-Sosa, U. Lemmer, U. W. Paetzold, *ACS Appl. Energy Mater.* **2018**, *1*, 1834.
- [155] S. Schliske, F. Mathies, D. Busko, N. Strobel, T. Rödlmeier, B. S. Richards, U. Lemmer, U. W. Paetzold, G. Hernandez-Sosa, E. Klampaftis, *ACS Appl. Energy Mater.* **2019**, *2*, 764.
- [156] T. Abzieher, S. Moghadamzadeh, F. Schackmar, H. Eggers, F. Sutterlüti, A. Farooq, D. Kojda, K. Habicht, R. Schmagel, A. Mertens, R. Azmi, L. Klohr, J. A. Schwenzer, M. Hetterich, U. Lemmer, B. S. Richards, M. Powalla, U. W. Paetzold, *Adv. Energy Mater.* **2019**, *9*, 1802995.
- [157] S. G. Hashmi, D. Martineau, X. Li, M. Ozkan, A. Tiihonen, M. I. Dar, T. Sarikka, S. M. Zakeeruddin, J. Paltakari, P. D. Lund, M. Grätzel, *Adv. Mater. Technol.* **2017**, *2*, 1600183.
- [158] S. G. Hashmi, A. Tiihonen, D. Martineau, M. Ozkan, P. Vivo, K. Kaunisto, V. Ulla, S. M. Zakeeruddin, *J. Mater. Chem. A* **2017**, *5*, 4797.
- [159] C. Trudeau, M. Bolduc, P. Beaupré, J. Benavides-guerrero, S. G. Cloutier, *MRS Adv.* **2018**, *3*, 1837.
- [160] A. J. Huckaba, Y. Lee, R. Xia, S. Paek, V. C. Bassetto, E. Oveisi, A. Lesch, S. Kinge, P. J. Dyson, H. Girault, M. K. Nazeeruddin, *Energy Technol.* **2019**, *7*, 317.
- [161] Saule Technologies, <https://sauletech.com/> (accessed: October 2019).
- [162] F. Mathies, P. P. Brenner, G. Hernandez-Sosa, I. A. Howard, U. W. Paetzold, U. Lemmer, *Opt. Express* **2018**, *26*, A144.
- [163] A. M. Alamri, S. Leung, M. Vaseem, A. Shamim, J.-H. He, *IEEE Trans. Electron Devices* **2019**, *66*, 2657.
- [164] J. Liu, B. Shabbir, C. Wang, T. Wan, Q. Ou, P. Yu, A. Tadich, X. Jiao, D. Chu, D. Qi, D. Li, R. Kan, Y. Huang, Y. Dong, J. Jasieniak, Y. Zhang, Q. Bao, *Adv. Mater.* **2019**, 1901644, 1901644.